



HAL
open science

Dynamics of core-mantle separation: Influence of viscosity contrast and metal/silicate partition coefficients on the chemical equilibrium

Vincent Clesi, Julien Monteux, B. Qaddah, M. Le Bars, J.-B. Wacheul,
Mohamed Ali Bouhifd

► To cite this version:

Vincent Clesi, Julien Monteux, B. Qaddah, M. Le Bars, J.-B. Wacheul, et al.. Dynamics of core-mantle separation: Influence of viscosity contrast and metal/silicate partition coefficients on the chemical equilibrium. *Physics of the Earth and Planetary Interiors*, 2020, 306, pp.106547. 10.1016/j.pepi.2020.106547 . hal-02933230

HAL Id: hal-02933230

<https://uca.hal.science/hal-02933230v1>

Submitted on 5 Nov 2020

HAL is a multi-disciplinary open access archive for the deposit and dissemination of scientific research documents, whether they are published or not. The documents may come from teaching and research institutions in France or abroad, or from public or private research centers.

L'archive ouverte pluridisciplinaire **HAL**, est destinée au dépôt et à la diffusion de documents scientifiques de niveau recherche, publiés ou non, émanant des établissements d'enseignement et de recherche français ou étrangers, des laboratoires publics ou privés.

1
2
3
4
5
6
7
8
9
10
11
12
13
14
15
16
17
18

Dynamics of core-mantle separation:

Influence of viscosity contrast and metal/silicate partition coefficients on the chemical equilibrium

V. Clesi^{a,*}, J. Monteux^a, B. Qaddah^{a,b}, M. Le Bars^b, J.-B. Wacheul^b, M.A. Bouhifd^a

^aUniversité Clermont Auvergne, CNRS, IRD, OPGC, Laboratoire Magmas et Volcans, F-63000 Clermont-Ferrand, France

^bCNRS, Aix Marseille Université, Centrale Marseille, Institut de Recherche sur les Phénomènes Hors Equilibre, UMR 7342, 49, Rue F. Joliot-Curie - B.P. 146, 13384 Marseille Cedex 13, France

*Corresponding author: vincent.clesi@univ-lyon1.fr

Present address: Laboratoire de Géologie de Lyon- Terre, Planètes, Environnement, CNRS UMR 5276, ENS de Lyon, Université Lyon 1. Campus de la Doua, Batiment Geode, 2 Rue Raphaël Dubois, 69622 Villeurbanne Cedex.

19 **Abstract**

20 The composition of the Earth's core and mantle is set by the chemical equilibrium between metals
21 and silicates during core/mantle segregation. The metallic core separated from the mantle by
22 gravitational descent in the form of diapirs in a magma ocean, and therefore the dynamics of the
23 diapir's downward movement has an influence on the chemical equilibrium. In this study, we
24 characterize the descent of metallic droplets into a molten silicate using numerical models. By
25 varying the silicate and metal viscosities (between 0.1 and 1000 Pa.s for each phase) as well as
26 the partition coefficient between metal and silicate ($D^{met/sil}$, varying between 1 and 1000), we
27 obtained quantifying parametrizing equations for the degree of equilibrium between molten metal
28 and molten silicate, in a regime characterized by low We ($We < 10$) and low Re ($10^{-3} < Re < 10^2$).
29 We showed that the main parameters controlling the equilibrium for a siderophile element are the
30 viscosity of the silicate and the partition coefficient. We applied our parameterization for Ni and
31 Co in the context of late accretion on Earth so as to quantify the variation of the Ni/Co ratio after
32 a large impact as a function of the magma ocean viscosity, for an iron-rain scenario of
33 metal/silicate segregation. Using previous models (Canup, 2004) of the Moon-forming impact,
34 we showed that the Moon formation had an effect on the current Ni/Co ratio. Depending on the
35 radius of Theia's core and the viscosity of the magma ocean produced after the impact between
36 the proto-Earth and Theia, the Moon formation could account for 0.45 % to 3 % of the current
37 Ni/Co ratio for magma ocean viscosities of 0.1 to 100 Pa.s, respectively.

38

39

40 **1. Introduction**

41 The main process occurring on Earth during the first 100-150 million years was the
42 segregation of its metallic Fe-rich core (*e.g.* [Bouhifd et al., 2017](#); [Rubie et al., 2015](#); [Wood
43 et al., 2006](#); and references therein). One major consequence of this segregation is the
44 depletion of the Earth's mantle in the siderophile elements relative to primitive solar
45 system abundances (*e.g.* [Jones and Drake, 1986](#)).

46 The most recent Earth core formation models include a combination of multistage
47 core-mantle differentiation with N-body accretion simulations, combined with continuous
48 Earth core formation where pressure, temperature, oxygen fugacity and chemical
49 composition of both the mantle and core vary during accretion of the Earth (*e.g.* [Rubie et
50 al., 2015](#), and references therein). These models consider that the accretion of the Earth
51 occurred during a series of large impact events (*e.g.* [Canup, 2008](#); [Wetherill, 1985](#);
52 [O'Brien et al., 2006](#); [Monteux et al., 2009](#); [Nakajima and Stevenson, 2015](#)). More
53 importantly, these models provide results for the metal-silicate partitioning of a significant
54 number of siderophile elements, which are consistent with observed mantle abundances
55 given that the oxygen fugacity increases from about IW-5 to IW-2 (5 to 2 log units lower
56 than the Iron-Wüstite buffer) during core segregation (*e.g.* [Cartier et al., 2014](#); [Rubie et
57 al., 2015](#); [Wade and Wood, 2005](#)).

58 In this context, the behavior of Ni and Co (two refractory and moderately siderophile
59 elements) has been considered to provide an important indication of the conditions of

60 Earth core formation. The consensus is now that metal-silicate equilibration at high
61 pressure, in the range of 40 – 60 GPa (corresponding to depths of 1000 – 1500 km), was
62 required to produce the observed Ni and Co depletions in the mantle ([Bouhifd and](#)
63 [Jephcoat, 2011](#); [Siebert et al., 2012](#); [Righter, 2011](#); [Fischer et al., 2015](#); [Clesi et al., 2016](#),
64 for some of the most recent studies). Similar conclusions were reached based on the metal-
65 silicate partitioning of lithophile and weakly-siderophile elements (*e.g.* [Mann et al., 2009](#)).
66 One can note here that the conditions of Earth core formation as derived from metal-
67 silicate partitioning of several elements cannot be used as an argument for single-stage
68 core formation. This is highly unlikely given that Earth core formation occurred over a
69 series of large impact events.

70 Most core formation models are based on metal-silicate partitioning experiments
71 where both phases are fully molten and both thermodynamic and kinetic equilibrium are
72 reached. This type of scenario favors rapid core - mantle segregation, which is confirmed
73 by isotopic studies on Hf/W and short lived isotopes ([Kleine et al., 2002](#); [Jacobsen et al.,](#)
74 [2008](#)). If the kinetic equilibrium is well constrained, the extent to which the mantle and
75 core equilibrate with each other is model dependent. So we know that if the metal were to
76 segregate by forming large diapirs descending through the silicate magma ocean, the
77 timescale for the equilibration would be too long to explain the isotopic ratios of Hf/W
78 ([Rubie et al., 2003](#)). Therefore, the metal could have segregated by forming smaller
79 diapirs, or droplets, whose radius varied between 0.1 to 10 cm, forming a cloud of iron in

80 the magma ocean (Deguen et al., 2014; Wacheul et al., 2014). An intermediate scenario
81 combining iron-rain mingling for the first part of segregation in the magma ocean,
82 followed by creation of large descending diapirs also exists, which can explain the
83 equilibrium in a deep magma ocean. In such a scenario, the metal falls through the molten
84 silicate in the form of droplets, and then forms a metallic pond at the base of the magma
85 ocean. Gravitational instability then allows metal to form large diapirs which descend
86 through the solid layer of the mantle into the proto-core (*e.g.* Stevenson, 1981, Monteux
87 et al., 2015, Fleck et al., 2018). This study focuses on the iron-rain phase of core-mantle
88 segregation, during which chemical equilibrium is reached (Rubie et al., 2003, 2011), as
89 large diapirs have less chemical interaction with the surrounding fluid (Ulvrova et al.,
90 2011; Wacheul et al., 2014). In the scenario of segregation by iron rain (Fig. 1), the extent
91 to which the magma ocean is in equilibrium with the core depends on the properties of the
92 metallic flow. The physics of the fluid flow is dependent on various parameters, one of the
93 most important being the viscosity of the surrounding fluid (Ke and Solomatov, 2009;
94 Monteux et al., 2009; Ricard et al., 2009). Numerical and analog simulations of a metallic
95 diapir descending through a surrounding fluid with different viscosities have shown that
96 the diapir is more stable when surrounding viscosity increases from low values ($\sim 10^{-1}$
97 Pa.s) to high values (~ 100 Pa.s), (Samuel, 2012; Wacheul et al., 2014). This has an impact
98 on chemical equilibrium, since break-up of the diapir increases the surface of exchange
99 between metal and silicate and small droplets sink more slowly than large diapirs (Ulvrova

100 [et al., 2011](#); [Wacheul et al., 2014](#)). The efficiency of equilibrium is also increased when
101 internal convection favors homogenization of concentrations in the metallic droplets
102 ([Ulvrova et al., 2011](#)).

103 The goal of the present study is to characterize the influence of viscosity (metal and
104 silicate phases) and chemical equilibrium on the global equilibrium rate in a magma ocean.
105 To do that, the most relevant methods are analog and numerical modeling (e.g. [Samuel](#)
106 [and Tackley, 2008](#); [Sramek et al., 2010](#); [Deguen et al., 2011](#); [Wacheul et al., 2014](#)).
107 Numerical simulations are more practical than analog ones for studying the effects of
108 different phenomena happening simultaneously. In addition, it is difficult to find analogs
109 for both metal and silicate which will react exactly like these two phases, and even more
110 complicated to find analogs that behave chemically and physically in the same way as
111 molten metal and molten silicate. Given the limitations of analog experiments for multiple
112 physical modeling, we chose to perform numerical simulations of a falling metallic sphere
113 into a molten silicate using COMSOL Multiphysics 5.0 modeling software. This approach
114 allows the chemical equilibrium for different types of siderophile elements to be
115 determined. In our simulations we combined chemical diffusion calculations with different
116 types of flow. In particular, these simulations led us to explore the contamination of a
117 silicate column by an excess of a siderophile element initially present in the diapir. Since
118 viscosity influences the type of flow, which in turn is crucial in core-mantle equilibrium
119 modeling ([Rubie et al., 2003](#); [2011](#); [Samuel, 2012](#)), viscosity must have an influence on

120 the extent of core-mantle equilibrium. Furthermore, the equilibrium depends on the
121 partition coefficients of the elements between metal and silicate ($D^{\text{met/sil}}$), which depend
122 on pressure, temperature, oxygen fugacity and composition of metal and silicate.
123 Therefore, we tested the contamination of silicate by generic siderophile elements using
124 four different values of $D^{\text{met/sil}}$ (1, 10, 100, 1000).

125 Since major chemical transfers likely occurred during the iron rain process ([Rubie et](#)
126 [al., 2003](#)) our simulations looked at the equilibrium of droplets with the surrounding
127 silicate. In general, large diapirs in a turbulent environment tend to break into small
128 droplets, forming a cloud in which each droplet moves at the same speed ([Wacheul and](#)
129 [Le Bars, 2017, 2018](#)). In this study, we look at how one droplet of a given radius ($R_{\text{Fe}} = 1$
130 cm), which can be deformed but cannot break (see [Wacheul et al., 2014](#)), interacts with
131 the surrounding silicate. Then this behavior is extrapolated to the entire droplet cloud, and
132 we can estimate the extent to which equilibrium is reached between the magma ocean and
133 the falling metal during planetary accretion.

134 As a result of these simulations, we constrain the chemical exchanges between a small
135 metallic diapir and a silicate volume as a function of silicate viscosity (varying from 0.1
136 Pa.s to 1000 Pa.s), the viscosity ratio between metal and silicate, and time. We thus
137 parameterize the effect of varying viscosity on metal-silicate equilibration, and we use this
138 parameterization to re-evaluate models of core-mantle segregation. Moreover, we
139 characterize the effect of changing the magma ocean viscosity on the chemical

140 composition of the mantle. Finally, we discuss the potential consequences of giant impacts
141 such as the Moon-forming impact on the chemical composition of the Earth’s mantle.

142

143 **2. Physical Model**

144 To model the sinking of a metallic droplet into a silicate liquid, we used the software
145 COMSOL Multiphysics, and in particular the modules “Computational Fluids Dynamics”
146 and “Chemical Reaction Engineering”. In each module, a set of equations is defined and
147 solved at each time step. These equations are described in the following subsections. The
148 parameters we used for these equations are listed in Table 1.

149

150 **2.1. Two-phase flow model**

151 In our study, the fluid dynamics are governed by the Navier-Stokes equations that
152 characterize:

- 153 • Conservation of mass

$$154 \quad \nabla \cdot \mathbf{u} = 0 \quad (1)$$

- 155 • Conservation of momentum

$$156 \quad \rho \frac{\partial \mathbf{u}}{\partial t} + \rho(\mathbf{u} \cdot \nabla)\mathbf{u} = -\nabla P \mathbf{I} + \nabla \cdot [\mu(\nabla \mathbf{u} + (\nabla \mathbf{u})^T)] + \rho \mathbf{g} + \mathbf{F}_{st} \quad (2)$$

157

158 Equation 1 is the conservation of mass for an incompressible fluid with \mathbf{u} the flow
 159 velocity **vector**. Equation 2 describes the conservation of momentum, with acceleration of
 160 the fluid ($\frac{\partial \mathbf{u}}{\partial t}$) and an inertia term ($\rho(\mathbf{u} \cdot \nabla)\mathbf{u}$) where ρ is fluid density. The first term on
 161 the right-hand side of Eq. 2 ($-\nabla P$) is the effect of the dynamic pressure P on the fluid.
 162 The second term ($\nabla \cdot [\mu(\nabla \mathbf{u} + (\nabla \mathbf{u})^T)]$) is the component representing the effect of
 163 viscous forces on the fluid with μ the fluid viscosity. The third term ($\rho \mathbf{g}$) is the
 164 gravitational force that applies to the whole domain with \mathbf{g} the gravitational acceleration
 165 **vector**. The fourth term $\mathbf{F}_{st} = \nabla \cdot (\sigma(\mathbf{I} - \mathbf{nn}^T)\delta)$ is the surface tension force with σ the
 166 surface tension coefficient, \mathbf{I} the identity matrix, \mathbf{n} a unit vector normal to the surface of
 167 interest and δ a smeared out Dirac function located at the interface. Since the volume of
 168 metal is small, we ignored the Coriolis forces in Eq. 2.
 169 We monitored the interface between the liquid iron droplet and the molten silicates using
 170 the Level Set method, a Eulerian and implicit method used in multiphase flow problems
 171 (e.g. Qaddah et al., 2019). For that, we defined a function Φ , characterizing the silicate
 172 when $\Phi = 0$ and the metal when $\Phi = 1$. The boundary between the two phases was then
 173 set at $\Phi = 0.5$. These values were obtained by modifying the level set field using a smeared
 174 out Heaviside function (Olsson & Kreiss, 2005), which allows direct calculation of the
 175 volume fraction of a given phase by integration of the variable Φ on the volume
 176 considered. The equation governing the transport of Φ is:

177

178
$$\frac{\partial \Phi}{\partial t} + \mathbf{u} \cdot \nabla \Phi = \gamma \nabla \left(\epsilon_{ls} \nabla \Phi - \Phi(1 - \Phi) \frac{\nabla \Phi}{|\nabla \Phi|} \right) \quad (3)$$

179

180 with γ (m/s) and ϵ_{ls} (m) the reinitialization parameters. The γ parameter limits the
 181 numerical diffusion of the metallic phase during the simulation and needs to be adjusted
 182 empirically when the viscosity varies. Indeed, γ is a parameter that determines the amount
 183 of reinitialization or stabilization and must be carefully adjusted for each specific problem.
 184 If γ is too low, the thickness of the interface might not remain constant, and oscillations in
 185 Φ could appear because of numerical instabilities. On the other hand, if γ is too high, the
 186 interface moves incorrectly. The ideal value of γ was given by the maximum velocity
 187 reached by the diapir during its descent, as detailed in section 3. The range of values for γ
 188 is given in Table 1. ϵ_{ls} is the parameter controlling the width of the interface between
 189 fluids during reinitialization. This equation (Eq. 3) is a combination of the equations
 190 presented in [Olsson & Kreiss \(2005\)](#), modified for the COMSOL in-built solver. This
 191 solver allows the advection (on the left-hand side of the equation) and the reinitialization
 192 parameter (right-hand side of the equation) to be solved at the same time. The dynamic
 193 viscosity and the density are evaluated using the level set function and are defined by $\mu =$
 194 $\mu_{sil} + \Phi(\mu_{met} - \mu_{sil})$ and $\rho = \rho_{sil} + \Phi(\rho_{met} - \rho_{sil})$, respectively (subscript *met* refers
 195 to metal and *sil* to silicates). The resolution of the level set equation without using the
 196 COMSOL Multiphysics module is detailed in [Olsson & Kreiss, 2005](#). Furthermore, this
 197 method has been already validated and applied to a similar problem in [Qaddah et al., 2019](#).

198

199 The temperature of both the metallic droplets and the surrounding molten silicates is
200 difficult to constrain. It is related to the history of both phases before the merging and
201 involves radioactive heating, viscous dissipation and accretionary heating. In our study
202 we consider that the impact that precedes the iron droplet sinking homogenizes the
203 temperature of both phases. Hence, we do not consider heat conservation in the equations
204 solved in our models, and focus instead on the chemical equilibration processes alone.

205

206

207 **2.2. Chemical model**

208 The chemical diffusion and reactions of elements are described by transport equations
209 including an advective term to account for the movement of the phase and conservation of
210 mass, a diffusion term (Fick's law) to account for diffusive transfer, and a reaction term
211 to account for the chemical transfer based on the partition coefficient between metal and
212 silicate. In our models we solve the following equation:

$$213 \quad \frac{\partial c_i}{\partial t} + \nabla \cdot (-k_c \nabla c_i) + \mathbf{u} \cdot \nabla c_i = R_i \quad (4)$$

214 Eq. 4 is the transport equation for diluted species including Fick's law for the diffusion of
215 an element ($\nabla \cdot (-k_c \nabla c_i)$) with the addition of an advective term ($\mathbf{u} \cdot \nabla c_i$) to account for

216 motions within the fluids. c_i is the concentration of element i in the phase of interest, k_c the
217 diffusion coefficient and R_i the reaction rate for element i .

218 In our case, there are no external sources of elements ($N_i=0$, Fig. 2).

219

220 We assumed the diffusion coefficient (k_c) to be the same for both phases, and independent
221 of the partition coefficient (D_i). Therefore we defined two functions to describe the
222 behavior of element i in each phase. One function (X_i^{sil}) describes the behavior of element
223 i in the silicate, and therefore tends toward 0 when $\Phi = 1$, the other (X_i^{met}) described the
224 behavior of element i in the metal and tends toward 0 when $\Phi = 0$. The combination of the
225 two functions give us the global concentration of element i in our computational domain.

226 The link between the two functions, the partitioning coefficient and the phase field is made
227 by defining a reaction at the interface between the metal and silicate (i.e. when $\Phi = 0.5$):

228 R_i is the reaction rate necessary to reach the chemical equilibrium defined by the metal-
229 silicate partition coefficient of element i (D_i). D_i is the Nernst partition coefficient given

230 by $D_i = \frac{X_i^{met}}{X_i^{sil}}$, where X_i^{met} is the mass fraction of element i in the metallic phase, and X_i^{sil}

231 the mass fraction of the same element in the silicate phase at equilibrium. R_i is given by

232 Eq. 5:

$$233 \quad \frac{dc_i}{dt} = R_i \quad (5)$$

234 Where c_i is the concentration in either silicate or metal in mol.m^{-3} , obtained from the
235 density of the phase where the element is ρ^{phase} (for either a metal or silicate phase), the

236 molar mass of the element (M_i) and the mass fraction of the element i in the phase
237 considered is represented by $c_i = \frac{X_i^{phase} \rho^{phase}}{M_i}$. R_i is automatically calculated in a
238 stationary state from the initial conditions and a given partition coefficient so as to reach
239 equilibrium using COMSOL's in-built solver before the simulation. The reaction rate is
240 high enough to maintain the equilibrium between two calculation steps: the typical time
241 for equilibration is 10^{-5} s, which is less than the time step solved by solver. R_i is negative
242 when removing siderophile elements from the metallic phase, and positive when creating
243 the same element in the silicate phase. The reaction function is only defined for the
244 metal/silicate boundary, given by the condition $\Phi = 0.5$. The higher the value of $D_i^{met/sil}$,
245 the closer the conditions are to equilibrium, and the lower the reaction rate (R_i) will be.
246 For the domain where $\Phi = 0$ or 1 , the equilibrium is set to 0 , and therefore the reaction
247 rate is 0 . For a given time step, the in-built COMSOL Multiphysics 5.0 solver calculate
248 the Navier-Stokes equations (Eqs. 1 and 2) using finite element method, yielding the
249 velocity field. Then the level-set equation is computed at the same time the advection-
250 diffusion (Eq. 4) equation is solved by finite-element methods on the entire computational
251 domain, with the reaction R_i only defined where $\Phi = 0.5$. The results of the calculation
252 are then used as starting condition for the next time step.

253

254 **2.3. Geometry, mesh and initial conditions**

255 First, we defined a geometry for the simulation, using one of the defined boundaries
256 for the eulerian solver available with COMSOL Multiphysics 5.0 software geometries.
257 The best choice for our type of simulation would have been be a 3-D model with a falling
258 sphere inside it, so as to compare our simulation to analog simulations ([Deguen et al.,](#)
259 [2011, 2014](#); [Wacheul et al., 2014](#)). Since this type of simulation is very costly in terms of
260 computational time, especially for fluid flow simulations, we used a 2D-axisymmetric
261 geometry, which solves the equation on a 2D surface, and uses the symmetry conditions
262 to give a 3D output. This is a good compromise between a 2D and 3D simulation when
263 the diapir is not fragmented. Our simulations focused on a weakly deformable falling
264 sphere (i.e. no break up) with a radius of 1 cm in a cylinder whose diameter was set during
265 the calibration of the simulation.

266

267 The geometry and boundary conditions used in this study are presented in Fig. 2. In
268 this geometry, a rotational symmetry axis is defined. For the fluid flow, the boundaries of
269 our calculation domain are characterized as follows:

- 270 - on the top boundary, the condition is given by $P= 1 \text{ atm}$,
- 271 - on the bottom boundary, the condition is set to be a null velocity field
- 272 - on the side boundary, the condition is a no slip condition
- 273 - on all the boundary there is a no flow condition for the level set equation.

274 The conditions for chemical diffusion is a constant budget in chemical elements
275 throughout the numerical simulation, i.e. no elemental flux ($N_i = 0$), inward or outward, is
276 allowed on all the external boundaries.

277 For our calculation domain we used a fixed mesh of triangles, with three main
278 parameters: h_{\max} , h_{\min} and a curving parameter. The h_{\max} parameter gives the maximum
279 size of the triangle side, h_{\min} gives the minimum size and the curving parameter gives the
280 arc interception for curving triangles at spherical boundaries. The parameter controlling
281 the accuracy and the computation time for the calculation is h_{\max} . The best value for this
282 parameter was determined in the resolution study, see Section 2.4.

283 The initial conditions are described in Fig. 2. The viscosities were varied for each
284 simulation, but the geometry of the set-up, the initial concentrations, the densities and the
285 droplet radius were kept constant. To avoid numerical instabilities inherent in $X_{sil}^0 = 0$
286 %wt, the initial concentration was set to $X_{sil}^0 = 10^{-4}$ %wt for the silicate with a density ρ_{sil}
287 = 3300 kg.m⁻³; and $X_{met}^0 = 20$ % wt for the metal with a density $\rho_{met} = 8000$ kg.m⁻³. The
288 radius of the droplet was $R_{Fe} = 1$ cm, falling in a cylinder with a 5 cm radius and a 28 cm
289 height, with the center of the droplet placed initially at 26 cm height.

290

291 **2.4. Tests of the COMSOL simulation**

292 To correctly set up the computational domain in terms of size and mesh, two effects
293 need to be accounted for:

294 (1) Grid resolution, which has to be sufficient to capture the physics of small droplet
295 deformation.

296 (2) Boundary effects, to avoid a major influence of the outer border of the domain on
297 the flow and the generation of artifacts in the velocity field.

298 To minimize the numerical diffusion of iron during the diapir's descent, we tested several
299 maximum sizes for the mesh grid component h_{\max} . Fig. 3 illustrates the time evolution of
300 the ratio between the calculated volume over the theoretical volume of one droplet (given
301 by $V_{\text{theoretical}} = \frac{4}{3} \pi R_{\text{Fe}}^3$ with $R_{\text{Fe}}=1\text{cm}$) for h_{\max} values ranging between 0.06 and 0.2 cm.

302 The simulations were performed using the same initial geometry as in Fig. 2, with a silicate
303 and a metal viscosity of 100 Pa.s (corresponding to a Reynolds number of $\sim 2 \cdot 10^{-3}$, see
304 Eq. 6) and no chemical component to solve. The precision of the calculation increased as
305 the mesh size decreased, especially when there was deformation. On the other hand, the
306 smaller the mesh grid components were, the longer it took to complete the calculation. As
307 can be seen in Fig. 3, the precision is better for a mesh component size of 0.1 cm than for
308 smaller (0.06 and 0.08 cm) or larger (0.2 cm) mesh component sizes. In addition, a
309 maximum component size allowed a calculation time of a few hours (~ 6 hours), whereas

310 a mesh grid size of 0.06 cm yielded calculation times from a dozen hours to 2 days for the
311 less viscous flows. Therefore, for the rest of the study, we used a maximum size of 0.1 cm
312 for the mesh grid (i.e. $R_{Fe}/10$). The mesh size could be adapted to the type of flow for each
313 simulation: for example, for a higher degree of diapir deformation during the simulation
314 (typically for less viscous flows), the mesh size had to be decreased to avoid numerical
315 artifacts. To increase the precision, COMSOL also made it possible to set a minimum size
316 for the mesh grid component so as to get an adapted mesh, with smaller elements at the
317 interfaces between the two phases, and larger elements as the distance from the interface
318 increases. Varying the parameter h_{min} did not affect the simulation for a given value of
319 h_{max} , so it was kept at a constant value of $h_{min} = h_{max}/40$.

320

321 The second point was to avoid boundary effects on the fluid flow during the simulation.
322 We tested several domain sizes and checked the different velocity field components (r-
323 and z- components). We chose a height equal to $28 \times R_{Fe}$ and a width equal to $5 \times R_{Fe}$ which
324 was sufficient to avoid the recirculating flow associated to the descending diapir having a
325 large effect on the velocity field (Fig. 4), while keeping computational time within
326 reasonable bounds. This size of domain still affected the velocity of the diapir (Chang,
327 1961 and Fig. 4). Fig. 4 shows that increasing the width to $6 \times R_{Fe}$ changed the velocity
328 field, albeit very slightly, which indicates a diminution of the wall effect: the mean
329 velocity of the diapir increased by 8 % compared to the mean velocity for a width of $5 \times R_{Fe}$.

330 However, increasing the width of the domain from $5xR_{Fe}$ to $6xR_{Fe}$ led to a significant
331 increase in computational time (by at least 46 %). Given the limited effect of increasing
332 the domain width and the significant effects on the computational time, we considered this
333 smaller width to be suitable for the study. We applied the same reasoning to choose the
334 height of our domain. To test the resolution of the diffusion in Eq. 4, we benchmarked the
335 validity of the COMSOL solver against steady and unsteady analytical solutions for
336 diffusion problems (Crank, 1975). To test the advective part, we compared the flow
337 velocities from our models with those velocities obtained by Samuel (2012) (see section
338 3.2). Our results showed an acceptable agreement, despite a large discrepancy between
339 theoretical results and observed velocities (45% for the largest one) for flows with the
340 largest velocities, i.e. in the intermediate regime. To explain the observed differences, we
341 calculated the mesh Peclet number Pe_{mesh} after each simulation with $Pe_{mesh} = \frac{vh_{max}}{k_c}$,
342 where v is the velocity of the diaphragm, h_{max} is the mesh size and k_c is the diffusion coefficient
343 ($10^{-6} \text{ m}^2 \cdot \text{s}^{-1}$, which is higher than a typical chemical diffusion, but high enough to limit
344 numerical diffusion (see Qaddah et al., 2020). In the reference case and for the other cases
345 within the Stokes regime, the value of Pe_{mesh} was sufficiently low ($Pe_{mesh} < 10$) meaning
346 that numerical diffusion was negligible (see Mittal & Jain, 2012). For the cases within the
347 intermediate regime, Pe_{mesh} was higher ($Pe_{mesh} > 50$), which indicates possible numerical
348 diffusion that likely affected our results. To correct this effect a much smaller mesh size
349 would have been necessary. However, the mesh size necessary to prevent numerical

350 diffusion in our models would have led to unreasonable computational times. Therefore,
351 for the lowest viscosity used in our models some error calculations might have occurred
352 in our results, but are negligible in the final model (see Section 5 and 6).

353

354 **3. Results**

355 In this section we present the results of our simulations as well as a definition of the non-
356 dimensional numbers and parameters used to interpret the results of the simulation in
357 terms of degree of equilibrium. A reference run was arbitrarily defined to set a reference
358 time evolution for the non-dimensional parameters. Then we varied the viscosity of the
359 silicate and metallic phase for a given partition coefficient value, and finally we varied the
360 value of the partition coefficient for a given viscosity.

361

362 **3.1. Reference case and characteristic non-dimensional numbers**

363 In this section we present the results for a reference case, where $\mu_{sil} = \mu_{met} = 100$ Pa.s.
364 The temporal evolution of the reference case flow is presented in Fig. 5. This figure shows
365 that for this case both the diapir deformation and the numerical diffusion are weak. The
366 metallic droplet moves a distance of $10 \times R_{Fe}$ (10 cm) in 12.1 seconds.

367

368

369 To compare this flow to other flows with different viscosities, we need to use non-
370 dimensional numbers. Since this study focuses on the viscosity variations and the
371 characteristics of the flow, the Reynolds number (Re) is the more adequate non-
372 dimensional number, which is given by Eq. 6:

373

$$374 \quad Re = \frac{\rho_{sil} R_{Fe} v_{diapir}}{\mu_{sil}} \quad (6)$$

375 where ρ_{sil} is the density of the surrounding silicate, R_{Fe} is the initial radius of the diapir,
376 v_{diapir} is the velocity of the diapir and μ_{sil} is the silicate viscosity (see Table 1). This number
377 expresses the ratio of inertial forces to viscous forces. When $Re < 1$, the flow is considered
378 to be a Stokes flow, which means that diapir deformation is limited during the descent.
379 When $1 < Re < 500$, the flow is an intermediate flow between Newtonian and Stokes flow
380 (Samuel, 2012). In our study, we did not investigate the case of $Re > 500$, which is a highly
381 turbulent Newtonian flow.

382

383 The velocity of the diapir is strongly governed by the viscosity of the surrounding silicate,
384 which affects the value of Re (e.g. Samuel, 2012, and references therein). In order to
385 compare different values of the viscosity ratio $R_{\mu} = \mu_{met} / \mu_{sil}$, we defined the reference
386 time for each calculation as the time necessary for a metallic droplet with radius R_{Fe} to
387 move through a distance $d=10 \times R_{Fe}$.

388 The other non-dimensional number which controls the flow is the Weber number
389 (We), which is the ratio of the inertial forces on the surface tension:

390
$$We = \frac{\rho_{sil} v_{diapir}^2 R_{Fe}}{\sigma} \quad (7)$$

391 with σ the surface tension (see Tab. 1 for value). The break-up of the diapir is controlled
392 by the Weber number (Wacheul et al., 2014). When $We < 6$ the diapir is stable in Stokes
393 and intermediate flows, and when $We > 6$ the surface tension is no longer high enough to
394 prevent the diapir breaking up (Wacheul and Le Bars, 2017). In this case and in the rest of
395 the present study, the diapirs are always stable with $We < 6$. For the reference case, the
396 diapir velocity is about $v_{diapir} \approx 8 \times 10^{-3} \text{ m.s}^{-1}$. This velocity yields low values of Re and We
397 (2.2×10^{-3} and 1.2×10^{-3} , respectively), which explains the diapir's stability during its
398 descent (see Fig. 5).

399

400 To study the chemical equilibrium between metal and silicate, we calculated a non-
401 dimensional concentration, or more precisely a non-dimensional mass fraction termed X' .
402 This non dimensional mass fraction was calculated so as to satisfy three conditions:

- 403 (i) If there is no change in the initial concentration in the silicate, X' is equal to 0
404 (no equilibrium at all)
- 405 (ii) If equilibrium is reached, X' is equal to 1.
- 406 (iii) X' is proportional to the concentration in the silicate ($X' \propto X$)

407 The first condition is reached if $X = X_{sil}^0$. Therefore $X' = 0$ implies a null numerator for
408 X' , i.e. $X' \propto X - X_{sil}^0$. For the second condition, it is reached if $X = X_{met}^{eq} / D_{met/sil}$, by
409 definition of the partition coefficient, where X_{met}^{eq} is the concentration of the element in
410 the metallic phase at equilibrium. In our case, the element is a siderophile ($D_{met/sil} \geq 1$)
411 and the initial concentration is high ($X_{met}^0 = 0.2$). Therefore, at the end of the simulation
412 we could approximate the equilibrium concentration by $X_{met}^{eq} \sim X_{met}^0$. Satisfying the
413 condition $X' = 1$, with $X' \propto X - X_{sil}^0$ and the non-dimensionality of X' yield to the
414 following formula given in Eq. 8:

$$415 \quad X' = \frac{X - X_{sil}^0}{X_{met}^0 / D_{met/sil} - X_{sil}^0} \quad (8)$$

416 X' is a useful parameter for tracking the evolution of concentration in a particular case,
417 but it is not enough to quantify how much of the silicate is affected by a change in
418 concentration. Moreover, this parameter is not suitable for comparing different studies,
419 because it is strongly affected by the duration of the sinking. The evolution of the non-
420 dimensional concentration, X' , in the reference case is shown in Fig. 6. Equilibrium in the
421 silicate is reached when $X' = 1$ (area in red). This area forms a very narrow zone around
422 the diapir, and most of the silicate is not chemically equilibrated with the metal, because
423 the simulation run time is not long enough.

424 The parameter R_C is the ratio of the silicate volume that has reacted with the metal to the
425 total volume of silicate. The definition is $R_C = V_{reacted}^{sil} / V_{total}^{sil}$, where $V_{reacted}^{sil}$ is the

426 volume of silicate where $X > X_{sil}^0$; meaning R_C is the volume fraction of silicate that has
427 reacted with the metal. To visualize how the ratio is calculated, a representation of the
428 integrated volume is shown in Fig. 7. In this figure, the areas colored in red represent the
429 volume of silicate that has evolved in terms of chemical composition, while the areas in
430 blue represent that which has not been contaminated by the diapir's descent.

431 For each simulation, the volume chemically affected by the diapir's descent increases with
432 time. The time evolution of the R_C value for the reference case is shown in Fig. 8. R_C is
433 increasing with time following the same trend in each case. The difference is in the
434 absolute values of $D^{met/sil}$: the more elevated the value is, the closer the initial conditions
435 are to equilibrium conditions, which leads to a lower reaction rate.

436

437

438 **3.2. Range of Re and We values**

439 The aim of our models was to constrain the influence of the viscosity contrast between
440 the silicate and metallic phases. This led to a wide range of Re and We values in our
441 numerical simulations. The viscosity of the silicates surrounding the metal droplet controls
442 the flow regime and the sinking velocity. The evolution of the time necessary to reach the

443 distance of $10 \times R_{Fe}$, which depends mostly on the silicate viscosity (Samuel, 2012 and
 444 references therein), is presented in Fig. 9. The higher the viscosity of the silicate, the longer
 445 it takes for the diapir to reach a set distance. The changes in flow regime result in different
 446 expressions for the diapir velocity. In our study, the range of Re values only allows Stokes
 447 regime flows ($Re < 1$) or intermediate regime flows ($1 < Re < 500$), with two different
 448 expressions for the diapir's velocity. In a Stokes flow the velocity is given by:

$$449 \quad v_{Stokes} = \frac{2}{9} \frac{(\rho_{met} - \rho_{sil})gR_{Fe}^2}{\mu_{sil}} \quad (9)$$

450 For intermediate flows, the sinking velocity is given by:

$$451 \quad v_{intermediate} = \sqrt{\frac{2(\rho_{met} - \rho_{sil})gR_{Fe}}{\rho_{sil}C_D}} \quad (10)$$

452 with C_D the drag coefficient. In our case, the drag coefficient is approximated by $C_D =$
 453 $\frac{12}{Re} + 0.3$, following Samuel (2012). From Eq. 10, we can also calculate the velocity in
 454 each drop flow regime: Stokes, intermediate, and Newton (e.g. Qaddah et al., 2019). The
 455 theoretical times associated with the velocity are compared to the actual times observed in
 456 simulations in Fig. 9. It shows a good agreement between theoretical and observed diapir
 457 velocity, despite some scatter. This scatter is consistent with the wall effect of our
 458 simulations: the variation in velocity observed in the Stokes flow is of the order of 10 %,
 459 which is consistent with the variation expected if the wall effect is negligible (see Section
 460 2.4). Comparison with the typical equilibrium time from Wacheul et al. (2014) in Fig. 9
 461 shows that, except for the intermediate flows, the fall time chosen in our study is long

462 enough to reach full equilibrium (or more than 90 % of equilibrium in some cases) inside
463 the metal, leaving the silicate as the limiting phase for equilibrium. The dispersion of the
464 obtained reference time (Eqs. 8 and 9) in Fig. 9 for a chosen value of μ_{sil} is considered
465 therefore as a negligible discrepancy in the rest of the study.

466 In Fig. 10 we plot the Re values as a function of the We values for each simulation (i.e.
467 for each viscosity contrast used in our calculations). The velocity of the diapir (v_{diapir}) used
468 to calculate Re and We is determined from our numerical models by the time necessary for
469 the diapir to move through a distance of $10 \times R_{Fe}$. This time is dependent on the viscosity
470 and illustrated in Fig. 9. Fig. 10 (left) shows that in all our numerical simulations, the
471 metallic droplet is stable (i.e. no break up occurs) even though some models are in the
472 Stokes regime and others are in the Intermediate flow regime. In Fig. 10 (right) we
473 compare the range of values with the range of We and Re values relevant to the geological
474 context of a liquid metallic droplet sinking through a terrestrial magma ocean (Wacheul et
475 al., 2014). As shown in Fig. 10 (right), our range of values is limited compared to possible
476 geophysical values. Larger diapirs leading to high Re and We values are not considered in
477 our study, which focuses on small droplets in the iron rain scenario.

478

479 **3.3. Influence of the viscosity ratio**

480 The viscosity ratio is an important parameter controlling the dynamics of diapir
481 descent, both its shape (Qaddah et al., 2019) and stability (Wacheul et al., 2014). In this

482 section, we focus on the influence of the viscosity ratio $R_\mu (= \mu_{met}/\mu_{sil})$ by varying the value
483 of the silicate viscosity for a given metal viscosity. Changing the viscosity of metal affects
484 its ability to deform and, hence, its terminal velocity, but this effect is not as strong as the
485 change in velocity implied by a change in ambient viscosity. This behavior is consistent
486 with the equation of diapir velocity in Stokes and intermediate flows (Eqs. (9) and (10)),
487 and is strongly dependent on the silicate viscosity. It is visible in Fig. 9, where a decrease
488 in silicate viscosity from 1000 Pa.s to 10 Pa.s (Stokes flows) leads to an increase in sinking
489 velocity from 10^{-3} m.s⁻¹ to 0.1 m.s⁻¹ for a metal viscosity of 1 Pa.s. For a constant silicate
490 viscosity of 10 Pa.s, a decrease of the metallic viscosity from 1000 Pa.s to 0.1 Pa.s only
491 increases the velocity from 0.05 to 0.1 m.s⁻¹. The viscosity ratio influences the sinking
492 velocity and, hence, affects the Re number and the flow regime, but not as strongly as the
493 silicate viscosity.

494 Fig. 11 illustrates the influence of the Re number on the silicate volume chemically
495 contaminated during the sinking of a metallic droplet with $R_{Fe}=1$ cm. For each case, the
496 evolution of R_C is shown as a function of Re , and for a distance of 10 cm ($10 \times R_{Fe}$). The
497 time corresponding to this distance is shown in Fig. 5 as a function of viscosity. Except
498 for the case with $D^{met/sil} = 10^3$, there is no linear correlation between $\log(R_C)$ and $\log(Re)$.
499 However, we clearly show a transition between the Stokes regime and the Intermediate
500 regime. In the Stokes regime flow, an increasing Re (i.e. a decreasing value of μ_{sil}) leads
501 to a significant decrease of R_C , while R_C values seem to reach a plateau when the flow

502 reaches the intermediate flow regime. Fig. 11 also shows that the approximation made by
503 Rubie et al. (2003) to achieve an analytical solution for equilibrium is only valid for low
504 Re flows (high silicate viscosity). As the density of the silicate is not significantly altered
505 by the reaction, the parameter R_c (volume ratio of silicate equilibrated) can be compared
506 to their parameter F_s (mass ratio of silicate equilibrated). For the lowest Re value, there is
507 good agreement between our numerical data and the analytical calculation. However,
508 extrapolating the analytical solution to higher Re flows leads to an overestimation of the
509 equilibrated volume.

510 The R_c ratio is presented in Fig. 12 as a function of R_μ . A decrease in R_c is observed with
511 an increase in R_μ (i.e. a decrease of μ_{sil}) for a given viscosity of the metallic phase. For the
512 five parts of Fig. 12, which correspond to the five values of μ_{met} , the trend and the
513 magnitude of the values of R_c are quite similar, meaning that the effect of the viscosity
514 ratio is less important than the ambient viscosity, which governs the flow regime. For high
515 values of R_μ , the same plateau phenomenon as seen in Fig. 11 is observed, which
516 corresponds to lower silicate viscosity values (intermediate flow). In the Stokes regime,
517 the sinking velocity scales with μ_{sil}^{-1} (Eq. (9)) while in the intermediate regime, the sinking
518 velocity scales with C_D^{-1} . Given the expression of the drag coefficient (derived from
519 Samuel, 2012; see Section 3.2), and the expression of Re (Eq. (6)), the sinking velocity in
520 the intermediate regime scales with $(\rho_{sil}\mu_{sil})^{-0.5}$, as given by Eq. (10). Hence, R_μ has a

521 greater effect on Stokes flows than intermediate flows, because the changes in diapir
522 velocity are more pronounced for Stokes flows, as shown in Fig. 5.

523 Although the evolutions of R_C as a function of R_μ are quite similar in the five panels of
524 Fig. 12, some differences are noticeable. For the lowest values of μ_{met} , the R_C ratio
525 increases at high R_μ values while for high values of μ_{met} , the R_C ratio is nearly constant or
526 decreases with high R_μ (except for $D^{met/sil} = 1000$). This could be explained by the fact that
527 a higher viscosity ratio tends to stabilize the diapir and slow down its descent (Wacheul
528 et al., 2014). In a Stokes regime, it leads to an increase in the time necessary to reach the
529 same distance, in other words a longer reaction time; but in intermediate regimes this time
530 does not change significantly, while the diapir is less deformed, leading to a smaller
531 surface of exchange between metal and silicate. We illustrate this point in Fig. 13, for a
532 silicate viscosity of 0.1 Pa.s: the normalized surface of the diapir varies from 1 to 2.3 with
533 decreasing values of R_μ , which means that low R_μ for high Re (~ 100) values lead to an
534 increase of exchange surface by 130% relatively to the initial diapir surface. The same
535 effect is observed for $\mu_{sil} = 1$ Pa.s ($Re \sim 10$), to a lesser degree: for low metallic viscosity
536 ($R_\mu = 0.1$) the diapir surface increases by 20%. This leads to an increase in R_C value for all
537 partition coefficients except for $D^{met/sil} = 1000$, for which an increase in diapir surface has
538 a negligible effect, the deformation occurring over a short timescale at a low reaction rate.
539 This effect is weak in our study compared to the effect of Re and $D^{met/sil}$ (see Section 3.4),
540 because the We range of our study does not allow major diapir deformation. For the
541 deformation rate to have a strong impact on chemical equilibrium, the We values have to
542 be much higher ($We > 10$, see Lherm & Deguen, 2018).

543

544

545 **3.4. Influence of the partition coefficient**

546

547 We have shown in Figs. 11 and 12 that chemical equilibration was less efficient when the
548 value of the viscosity ratio between the iron and silicate phases was higher. This
549 conclusion also stands for the whole range of partition coefficients used in our models. As
550 detailed in Section 2.2, the higher the value of $D^{met/sil}$, the closer the conditions are to
551 equilibrium conditions, and the lower the reaction rate (R_i) will be. However, the
552 thermodynamical equilibrium is reached faster, which limits the amount of exchange
553 between the metallic droplet and the surrounding silicate. Therefore, the contaminated
554 volume represented by R_C decreases when $D^{met/sil}$ increases (see Figs. 11 and 12). This
555 effect is relatively small: an increase of 3 orders of magnitude decreases R_C by less than
556 one order of magnitude.

557

558 **3.5. Parameterization of the chemical contamination**

559 As shown in the previous sections, the contamination of silicate by a siderophile
560 element depends on the Reynolds number, viscosity ratio, and the values of metal-silicate
561 partition coefficients. To use our results in an iron rain scenario following an impact during
562 planetary formation, it is necessary to quantify the relative effect of each parameter on
563 chemical contamination. In section 3.1 and 3.2 we chose a distance of $10 \times R_{Fe}$ and the
564 relevant time (Fig. 5) at which R_C is considered to have reached a stationary value. With

565 this assumption the error is limited, since R_C tends to reach a plateau in all our simulations
 566 (see Fig. 8). Therefore, we consider the R_C values obtained from our models at a distance
 567 of $10 \times R_{Fe}$ in our parameterization.

568 We show in Sections 3.2 and 3.3 that increasing the Reynolds number and viscosity
 569 ratio both tend to decrease R_C . In Figs. 11 and 12, $\log(R_C)$ decreases linearly with both
 570 $\log(Re)$ and $\log(R_\mu)$ independently of the value of $D^{met/sil}$ with a small error in the prediction
 571 ($R^2 > 0.85 - 0.9$). Concerning the effect of partition coefficients, (Section 3.4), all the
 572 curves in Figs. 11 and 12 are parallel, showing that there is a linear relationship between
 573 $\log(R_C)$ and $\log(D^{met/sil})$. We parameterize the evolution of $\log(R_C)$ as a function of $\log Re$,
 574 $\log R_\mu$ and $\log D^{met/sil}$. The method used here is a multi-linear regression fit on all the data
 575 retrieved from the simulations:

$$576 \quad \log R_C = a \times \log D^{met/sil} + b \times \log Re + c \times \log R_\mu + d \quad (11)$$

577

578 where a , b , c and d are constants fitted to the data by least-square regressions. The values
 579 of the parameters are presented in Table 2. As shown in Fig. 14, the parameterization of
 580 Eq. (11) shows a relatively good fit to the data retrieved from calculations. This kind of fit
 581 is not perfect, and could certainly be improved by including non-linear dependencies. It is
 582 also worth noting that this parameterization is valid for a narrow range of Re and We
 583 values, and its precision is lower at high Re values (see section 2.4). For instance, different
 584 results can be found in turbulent cases (high Re , Deguen et al., 2014) and/or with deformed

585 diapirs (high We , [Lherm & Deguen, 2018](#)). However, this form of equation (Eq. (11)) is
586 practical to use in models of planetary formation with limited error on the value of R_C ,
587 therefore we chose this form to simplify the calculations in sections 5 and 6.

588 This parameterization shows that the main parameters controlling the
589 contamination of a liquid silicate reservoir by a siderophile element during the sinking of
590 a metallic droplet are the Reynolds number and the metal-silicate partition coefficients.
591 The higher the $D^{met/sil}$ is, the less the silicate will be contaminated, which reflects the fact
592 that we consider here a siderophile element. The Reynolds number has the same effect as
593 $D^{met/sil}$: the higher Re is, the lower R_C will be. This high absolute value of b reflects the
594 importance of the silicate viscosity, which controls the diapir velocity, as well as the type
595 of flow and the deformation of the diapir. The fact that the parameter b is negative shows
596 that increasing the value of the Reynolds number will decrease R_C . Indeed, decreasing the
597 viscosity increases the Reynolds number (Eq. 6) as well as the diapir velocity (*e.g.* [Samuel,](#)
598 [2012](#); [Wacheul et al., 2014](#), and Fig. 5).

599

600 **4. From a single droplet to the large impact context**

601 In the previous section, we derived a parameterization (Eq. 11) to estimate the volume
602 fraction of a magma ocean contaminated by a unique 1cm-radius metallic droplet. In this
603 section we apply this parameterization to large impacts in the context of late accretion.

604 The parameterization was calculated for a pertinent range of metallic and silicate
605 viscosities. Numerical simulations and laboratory experiments estimated the viscosity of
606 silicate melts at high pressure within the range of 0.01 Pa.s to 1 Pa.s. (Liebske et al., 2005;
607 Karki & Stixrude, 2010; Karki, 2018). This range is stable because the viscosity tends to
608 increase with pressure, but decrease with increasing temperature. As for the viscosity of
609 metallic liquid, few experiments have been made, but the experimental results also show
610 that the range of viscosity for liquid iron alloy is stable, at around 0.01-0.1 Pa.s (Kono et
611 al., 2015). Therefore, the effect of viscosity on the equilibrium rate calculated in our
612 simulation can be extrapolated for a high pressure context in an entirely liquid magma
613 ocean. The higher values (10 -1000 Pa.s) of μ_{sil} tested in our simulation can also be applied
614 at the end of the magma ocean stage when the silicate liquid is starting to crystallize (but
615 before the mushy stage where the flow dynamics is governed by the viscosity of the solid
616 silicate phase).

617 A more limiting factor to the extrapolation of our parameterization to planetary formation
618 is the size of our computational domain. However, it is possible under certain conditions,
619 which are listed below.

620 When a differentiated impactor collides with a growing planet, two fragmentation
621 mechanisms of its metallic core occur. The first fragmentation is induced by the impact
622 itself that stretches and disperses the impactor's core (Kendall and Melosh, 2016). The
623 lunar crater observations showed that the most probable impact angle is $\alpha = 45^\circ$

624 (Shoemaker, 1962). When considering an impactor with a metallic core radius of R_{core}
 625 impacting a magma ocean at an angle $\alpha = 45^\circ$, it is possible to apply our parameterization:
 626 the dispersion of the impactor's core material becomes the same as our study
 627 computational domain. The mantle fraction affected by the impact (i.e. the volume of
 628 mantle into which the metallic droplets are initially spread out) can be approximated by
 629 the volume of a cylindrical portion with an angle α , a thickness h and a radius L . The
 630 volume of mantle affected is then $V_{affected} = \alpha h L^2 / 2$. For $R_{imp}=100$ km, $R_{core}=50$ km,
 631 and $\alpha=\pi/4$, Kendall & Melosh (2016) give $h=200$ km, $L=2000$ km: we can then estimate
 632 $V_{affected} = 3.14 \times 10^{17}$ m³. After the first fragmentation induced by the impact, a second
 633 rapid fragmentation occurs leading to the formation of much smaller droplets of different
 634 sizes. Wacheul et al., (2014) showed that metallic diapirs will fragment into droplets with
 635 a mean radius of between 4 mm and 20 mm. Assuming an average droplet radius of 1 cm
 636 (Rubie et al., 2003) and that all the impactor's core diapir is fragmented into these cm-
 637 radius droplets, an impactor's core with radius $R_{core}=50$ km will fragment into $\approx 10^{20}$ cm-
 638 radius droplets. This yields a concentration of 400 droplets/m³, or 1 droplet per 2.5 liters,
 639 which yields a metal/silicate volume ratio of 0.0016 within $V_{affected}$. Currently, no scaling
 640 law describes the relation between (L, h, α) and R_{imp} (and as a consequence R_{core}).
 641 According to Kendall & Melosh (2016), for $R_{core}=50$ km, $L \approx 40R_{core}$ and $h \approx 4R_{core}$ and by
 642 making the assumption that these two relations are also valid for different R_{core} values, we

643 can infer that the ratio of the impactor's core volume over the affected volume is constant
644 for any impactor size.

645

646 In the numerical models described in the previous sections, we consider a metallic droplet
647 sinking into a large volume of molten silicates to avoid boundary effects. In our study the
648 ratio between the volume of the iron droplet and the volume of the computational domain
649 is 0.0019, which is relatively close to the volume ratio of 0.0016 expected after an impact.

650

651 After a large impact, the impactor's core is dispersed within a volume $V_{affected} =$
652 $\alpha h L^2 / 2$. Assuming the formation of a cloud of cm-radius droplets with an iron fraction
653 $\chi_{Fe} = 0.0016$ within $V_{affected}$, the volume where chemical exchange between the
654 droplets and the magma ocean will occur is:

655

$$656 \quad V_{exch} = R_c V_{affected} \quad (12)$$

657

658 Using Eq. (11), Tab. 2 and considering $L=40R_{core}$ and $h = 4R_{core}$ (Kendall and Melosh,
659 2016), we can calculate the fraction of the volume of the Earth's mantle V_{exch}/V_{mantle} in
660 which chemical exchange is likely to occur. Fig. 15 shows V_{exch}/V_{mantle} as a function of the
661 impactor radius and illustrates the influence of the partition coefficient and the viscosity
662 contrast between the magma ocean and the liquid iron on this ratio.

663

664 As the impactor size increases, the mantle volume chemically affected by the impact
665 increases by R_{imp}^3 . This relation is constrained by the simple formula we have used to
666 relate $V_{affected}$ to R_{core} . Given the current knowledge of the impact-induced fragmentation
667 mechanisms of an iron core on a planetary scale, this simplification is a first step toward
668 a global understanding of the chemical equilibration occurring after a large impact. Fig.
669 15 (left) illustrates that an increase in partition coefficient leads to a decrease in the ratio
670 V_{exch}/V_{mantle} in agreement with Eq. (11) and the values from Tab. 2. Fig. 15 (left) shows
671 that for $R_{core}=1000$ km, increasing the partition coefficient by 2 orders of magnitude
672 decreases the value of the ratio V_{exch}/V_{mantle} by a factor of 3. This effect is significant but
673 less important than the influence of the viscosity ratio. Fig. 15 (right) shows that
674 increasing the magma ocean viscosity relative to a constant liquid iron viscosity of 0.1
675 Pa.s from 0.1 Pa.s to 100 Pa.s leads to an increase in V_{exch}/V_{mantle} by a factor of more than
676 5. According to Fig. 15, a very large impact such as that which led to the formation of the
677 Moon-Earth system, involving a highly viscous magma ocean, would strongly enhance
678 the chemical equilibration between the impactor's core and the Earth's mantle. This result
679 needs to be nuanced, since a large impact is likely to increase temperature and therefore
680 lower the viscosity of the magma ocean.

681

682 **5. Signature of a large impact on the mantle composition**

683 This section aims at improving previous accretion models (e.g. [Fischer et al., 2015](#), [Siebert](#)
684 [et al., 2012](#), [Wood et al., 2008](#)) by accounting for a possible chemical disequilibrium at a
685 given depth. Previous models assumed that at a given step in accretion, equilibrium is
686 reached throughout the entire mantle ([Wood et al., 2008](#); [Siebert et al., 2012](#); [Boujibar et](#)
687 [al., 2014](#); [Clesi et al., 2016](#)). This equilibrium is set by the final pressure on reaching
688 equilibrium, usually at a depth corresponding to 50 % of the core mantle boundary depth
689 (or close to this depth, for instance in [Rubie et al., 2015](#)), in order to fit the Ni and Co
690 partitioning behavior ([Bouhifd & Jephcoat, 2003;2011](#); [Fischer et al., 2015](#)).

691 In this section and the following one, the hypothesis is the same as in previous models of
692 accretion, but with the notable exception that not all of the mantle reaches equilibrium.
693 The amount of mantle equilibrated is defined using Eqs. (11) and (12), i.e. our
694 parameterization is applied directly to a classical model of equilibration in a magma
695 ocean, thus adding one step of complexity to previous models.

696

697 **5.1. Geochemical elements of interest**

698 To estimate the chemical equilibrium between the impactor's core and the impacted
699 mantle, we focus our calculations on the chemical behavior of moderately siderophile
700 elements such as Ni and Co for which $D^{met/sil}$ is strongly dependent on pressure ([Bouhifd](#)
701 [& Jephcoat, 2003, 2011](#); [Siebert et al., 2012](#); [Fischer et al., 2015](#)). These two elements are
702 important, since the models of deep magma ocean are designed to explain their relatively
703 high abundances in the BSE ([Drake and Righter, 2002](#)). The maximum depth of the

704 magma ocean (around 50% the CMB depth throughout accretion) is derived from the
705 pressure for which the partitioning behavior of Ni and Co yields a 19.05 ± 2 ratio in the
706 BSE (Bouhifd & Jephcoat, 2003, 2011). In the previous sections, we considered a generic,
707 moderately siderophile element with a metal/silicate partition coefficient ranging from 1
708 to 1000. This range is large enough to extrapolate the trend derived from our simulations
709 to the behavior of Ni and Co at high pressure. For Ni, this partition coefficient ranges
710 between ≈ 400 for $P = 1$ GPa, and ≈ 20 for $40 < P < 60$ GPa. For Co, the partition coefficient
711 ranges between ≈ 100 for $P = 1$ GPa and ≈ 20 , for $40 < P < 60$ GPa (Bouhifd & Jephcoat,
712 2011 and references therein). In the models presented below, we assume that the pressure
713 of equilibrium after an impact corresponds to the last stages of equilibrium in a deep
714 magma ocean, at between 50 and 60 GPa (see Appendix B in Clesi et al., 2016 for the
715 corresponding calculations and the full evolution of pressure, temperature and f_{O_2} during
716 the accretion) with values of Ni and Co partition coefficients of between 20 and 80 for the
717 corresponding f_{O_2} . In the following section, we consider that the iron content of the mantle
718 is close to the BSE content (8% wt) and is not affected by the impact. The f_{O_2} is then
719 considered constant relatively to the iron-wüstite buffer and its value is $\log f_{O_2} \approx -2 \Delta IW$.
720 In this case, the Ni and Co partition coefficients have converged toward the same value:
721 $D^{met/sil} \approx 20$, which is used in the following calculations.

722

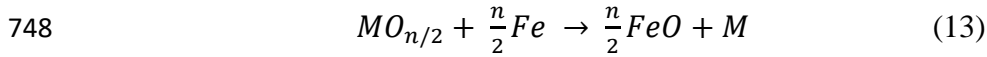
723 5.2. Chemical signature of a large impact on the Ni/Co ratio

724 Here we characterize the effect of a single impactor on the Ni/Co ratio in the mantle. We
725 consider an initially fully accreted Earth. The reference composition of the impacted
726 mantle is set to the BSE composition defined in [McDonough and Sun, \(1995\)](#) (Ni/Co =
727 19.05, 2000 ppm of Ni and 105 ppm of Co in the mantle). We consider that the silicate
728 fraction of the impactor is lost during impact and that only its metallic core is trapped
729 within the impacted mantle. The impactor has a radius of between 10 km and 1000 km
730 and the same composition as the Earth's core ([McDonough, 2003](#)). Given the range of
731 impactor size, the mass accreted is negligible compared to the Earth's mass: with a mean
732 density of 9400 kg.m^{-3} , a metallic impactor of 1000 km radius adds a total mass of $\sim 3.10^{22}$
733 kg, which is 0.5% of the Earth's mass. This choice of size and composition for the
734 impactor allows us to focus on the change in mantle concentration, without changing the
735 final core concentration, especially the light element (Si and S) content, in the core.
736 Furthermore, this impactor composition, and its relatively low mass, would not
737 significantly change the oxygen fugacity and thus does not affect the partitioning behavior
738 of Ni and Co.

739

740 This section aims at characterizing the partitioning behavior of Ni and Co as a function of
741 the impactor radius and the viscosity contrast R_μ computing Eqs. (11) and (12). The first
742 term of Eq. (11) illustrates the influence of the partition coefficients for Ni and Co. These

743 partition coefficients are controlled mainly by pressure and temperature, as well as the
 744 composition of the metallic phase, and oxygen fugacity (Bouhifd & Jephcoat, 2003, 2011,
 745 Siebert et al., 2012, Fischer et al., 2015). To obtain partitioning behavior independent of
 746 oxygen fugacity, we use the exchange partition coefficient K_d , which is the
 747 thermodynamical constant of the reaction:



749 Where M is the element considered (in our case Ni or Co), and n is the valence of the
 750 element M (in our case, n= 2). In reaction (13), the oxides are in the silicate phase, while
 751 the reduced element is in the metallic phase. The exchange partition coefficient is given

752 by $K_d = \frac{c_M}{c_{MO_{n/2}}} \times \left(\frac{c_{FeO}}{c_{Fe}}\right)^{n/2}$ where c_M and c_{Fe} are the molar fractions of M and Fe in the

753 metallic phase, and c_{FeO} and $c_{MO_{n/2}}$ are the molar fractions of FeO and $MO_{n/2}$ in the
 754 silicate phase. To estimate the values of the partition coefficients, we use the
 755 parameterization of K_d from Clesi et al., (2016), where we ignore the effect of water, as
 756 well as the carbon content in the metallic phase. The exchange partition coefficient, K_d , is
 757 given by:

758

$$759 \quad \log K_d^{element} = \frac{b_{el}}{T} + c_{el} \frac{P}{T} + e_{el} \log(1 - \chi_{Si}^{metal}) + g_{el} \log(1 - \chi_S^{metal}) + h_{el}$$

760 (14)

761

762 The parameters b_{el} , c_{el} , e_{el} , g_{el} and h_{el} are detailed in [Clesi et al., \(2016\)](#), and are different
763 for each element studied. P and T are the pressure (in GPa) and temperature (in Kelvin)
764 of equilibrium, respectively, corresponding to the pressure at 50% of CMB depth (i.e.,
765 1450 km), and the liquidus temperature associated with it ([Andrault et al., 2011](#)). We
766 assume here an equilibrium pressure of 63 GPa, and an equilibrium temperature of 3450
767 K. χ_{Si}^{metal} and χ_S^{metal} are the mass fractions of silicon and sulfur in the impactor. We
768 assume here that $\chi_{Si}^{metal} = 0.06$ and $\chi_S^{metal} = 0.019$ ([McDonough, 2003](#)). K_d is then
769 converted into a Nernst partition coefficient (mass ratio) following:

770

$$771 \quad D^{met/sil} = \frac{M_{oxide} \times M_{Fe}}{M_{FeO} \times M_{element}} \times K_d^{element} \times D_{Fe}^{met/sil} \quad (15)$$

772

773 where $M_{element}$ is the molar mass of Ni or Co, M_{oxide} is the molar mass of NiO or CoO, and
774 M_{Fe} and M_{FeO} are the molar masses of Fe and FeO respectively. $D_{Fe}^{met/sil}$ is the partition
775 coefficient of iron and equals 13.65 in the BSE model. We consider that the impactor does
776 not significantly change the oxygen fugacity and therefore does not influence the $D_{Fe}^{met/sil}$
777 value.

778 The second term in Eq. (11) characterizes the influence of the Reynolds number, which is
779 given by Eq. (6). As stated in Section 4, we consider that the metal fragments into droplets
780 with a radius of 1 cm. The sinking velocity of these droplets is given by Eq. (9). We
781 assume here a silicate density of $\rho_{mantle} = 4500 \text{ kg.m}^{-3}$ (mean density of the Earth's mantle),

782 a metallic density of $\rho_{metal}= 9400 \text{ kg.m}^{-3}$, which is consistent with iron rich liquid alloys
 783 at these pressures (Morard et al., 2013) and the current Earth's value for the acceleration
 784 of gravity (i.e., 9.81 m.s^{-2}). The viscosity of the silicate phase in our calculations ranges
 785 from 0.1 to 100 Pa.s. The third term in Eq. (11) measures the influence of the viscosity
 786 ratio $R_{\mu} = \mu_{met}/\mu_{sil}$. In our calculations, we consider a constant value for the metallic
 787 viscosity (= 0.1 Pa.s), consistent with iron liquid viscosity at high pressure (Kono et al.,
 788 2015).

789

790 Once the parameter R_C is calculated for Ni and Co, the impactor equilibrates with a volume
 791 of mantle defined by Eq. (12) in section 4, considering that $V_{impactor}/V_{affected} = 0.0016$,
 792 independent of the size of the impactor. As R_C expresses the volume fraction of the silicate
 793 that has reacted with the metal, it may overestimate the volume of the mantle that has
 794 equilibrated with the metal phase. Hence the parameter R_C should be considered as a first-
 795 order approximation of the volume equilibrated. Therefore, for Eq. (12), the mass of
 796 mantle that is equilibrated is obtained by simple multiplication by ρ_{mantle} . In this mass of
 797 mantle, the concentration of Ni or Co is in equilibrium and is given by $\chi_{eq}^{silicate} =$
 798 $\frac{\chi_{impactor}^{metal}}{D_{met/sil}}$. The final mass fraction of Ni or Co is given by:

799

$$800 \quad \chi_{final}^{silicate} = \chi_{initial}^{silicate} + (\chi_{eq}^{silicate} - \chi_{initial}^{silicate}) \frac{m_{equilibrated}}{m_{mantle}} \quad (16)$$

801

802 where, $\chi_{final}^{silicate}$ is the concentration of Ni or Co in the final mantle, $\chi_{initial}^{silicate}$ is the initial
803 concentration of Ni or Co in the mantle, $\chi_{eq}^{silicate}$ is the concentration at equilibrium,
804 $m_{equilibrated}$ is the mass that is equilibrated and m_{mantle} is the mass of the Earth's mantle. The
805 final Ni/Co ratio is then derived from $\chi_{final}^{silicate}$ for Ni and Co. The results of calculations
806 for different viscosities as a function of the impactor radius are presented in Fig. 16.

807

808 Fig. 16 shows that a single impactor, even a large one, does not significantly affect the
809 Ni/Co ratio in the mantle. The maximum variation is 0.25 %, and is obtained for a large
810 impactor (1000 km radius) for a relatively high viscosity of the magma ocean (100 Pa.s).
811 For low viscosities (0.1 and 1 Pa.s), a metallic impactor weakly affects the Ni/Co ratio in
812 the mantle (less than 0.1 % change for a 1000 km radius impactor). Such a small variation
813 confirms that high spatial resolution models are not necessary even for large Pe_{mesh} values
814 obtained for low viscosities. For a relative error of 100% in the values of R_c , at a viscosity
815 of 0.1 Pa.s, it would only induce a variation in Ni/Co of between 0 and 0.2% within the
816 final model.

817 Eq. (16) shows that the final concentration is proportional to the volume equilibrated if
818 $\chi_{eq}^{silicate}$ is higher than $\chi_{initial}^{silicate}$. In this case, late accretion of a metallic impactor, which
819 yields a high metallic concentration in Ni and Co (similar to the Earth core concentration
820 given in [McDonough, 2003](#)); with a high equilibrium pressure, which yields low partition
821 coefficient values for Ni and Co, $(\chi_{eq}^{silicate} - \chi_{initial}^{silicate})$ is positive. The impactor is

822 metallic and rich in Ni and Co (5.2%wt and 0.24 %wt, respectively), and impacts a silicate
823 mantle with a BSE composition. Therefore, when the mass of mantle equilibrated is
824 higher, the variation in Ni or Co concentration compared to the BSE in the mantle is
825 higher. If the disequilibrium is high, the $m_{equilibrated}$ is low, and therefore there is less
826 variation in the Ni/Co ratio. As shown in Fig. 16, the amount of disequilibrium is higher
827 for a low viscosity magma ocean, as well as for small metallic impactors, and therefore
828 there is no change in the moderately siderophile element concentrations in the mantle
829 under these conditions. This means that, to have a significant effect on the moderately
830 siderophile element concentrations in the BSE, late accretion impactors need to be large
831 and impact a viscous magma ocean in order to increase the degree of equilibrium. Even
832 in this case, if the amount of Ni and Co in the impactor is not significantly higher than that
833 in the Earth's core, the change in BSE composition will not be significant, as illustrated
834 in Fig. 16.

835

836 **6. Discussion**

837 **6.1. Earth accretion models and magma ocean properties**

838 In the previous section we characterized the effects of a late impact, negligible in mass,
839 composed only of a metallic phase. However, most of the disequilibrium happens during
840 accretion. Therefore, Eq. (16) is not relevant, at least not in this form, in the context of a
841 growing planet. Assuming that the mantle of the impactor and of the growing Earth is well

842 mixed before equilibration with the metallic fraction, we can define the concentration of
 843 the post-impact mantle, $\chi_{post-impact}^{silicate}$. By modifying Eq. (16), and knowing the
 844 composition of the impactor's metallic phase it is possible to calculate the composition of
 845 a growing planetary mantle before it equilibrates with the metallic phase of the impactor.
 846 It is given by:

$$847 \quad \chi_{post-impact}^{silicate} = \frac{m_{mantle}}{m_{mantle} - m_{equilibrated}} \left(\chi_{final}^{silicate} - \frac{m_{equilibrated}}{m_{mantle}} \chi_{equilibrated}^{silicate} \right) \quad (17)$$

848 Since $m_{equilibrated}$ is dependent on the size of the impactor core and magma ocean viscosity,
 849 it is possible to calculate the composition of the mantle for a 90% accreted Earth hit by a
 850 Mars-sized impactor (Moon-forming impact) as a function of the impactor's core radius
 851 and viscosity of the magma ocean. Fig. 17 shows the corresponding results for comparison
 852 with Fig. 16: in this case, the greater the degree of equilibrium, the lower the initial Ni/Co
 853 ratio.

854

855 The results displayed in Fig. 17 show that it is possible to reach the same final Ni/Co ratio
 856 for the Earth's mantle with drastically different properties of the impactor and the magma
 857 ocean. From Fig. 17, two post-impact models can be derived:

- 858 - A model with a low $R_{core}/R_{impactor}$ ratio and low magma ocean viscosity,
 859 which yields a lower degree of equilibrium between metal and silicate. In this kind
 860 of model, the composition of the Earth's mantle is more dependent on the
 861 equilibrium conditions between the metallic phase and the silicate phase than on

862 the composition of the impactor. For instance, the models presented in *e.g.* [Burbine](#)
863 [& O'Brien \(2004\)](#), [Rai & van Westrenen \(2013\)](#) or [Dauphas et al., \(2014\)](#) are based
864 on mixing different chondritic compositions where the main parameter fitted is the
865 isotopic consistency, and they are therefore predominantly compositionally-
866 derived models. For these models to be consistent, the impactor's core needs to be
867 small ($R_{core}/R_{impactor} < 0.4$, left-hand side of [Fig. 17](#)), and the magma ocean
868 viscosity low ($\mu_{magma\ ocean} \approx 0.1- 1$ Pa.s), so as to achieve a low equilibrium rate
869 between metal and silicate.

870 - A model with a high $R_{core}/R_{impactor}$ ratio, and high viscosity of the magma
871 ocean, which yields greater equilibrium between metal and silicate. In this kind of
872 model, the main changes in Earth mantle composition are due more to the
873 composition of the impactor and less to the chemical reactions between metal and
874 silicate. For instance, the models presented in *e.g.* [Wood et al., 2008](#), [Siebert et al.,](#)
875 [2012](#) and [Boujibar et al., 2014](#) are based on the metal-silicate partitioning behavior,
876 where the discriminating parameter is the relative core/mantle abundances of
877 siderophile elements, and they are therefore predominantly equilibrium-derived
878 models. In this kind of model, a minimal equilibrium needs to be reached, and
879 therefore the impactor's core needs to be large ($R_{core}/R_{impactor} > 0.4$, right-hand side
880 of [Fig. 17](#)), and/or the magma ocean viscosity needs to be high ($\mu_{magma\ ocean} \approx 10-$
881 100 Pa.s).

882 To summarize, our results cannot constrain the viscosity of the magma ocean (especially
883 given the error in our calculations for low viscosity calculations, see Section 2.4), but for
884 a given model, our results can constrain the range of magma ocean viscosities in order to
885 reach the BSE concentrations for moderately siderophile elements.

886 However, this work needs to be done for each accretion step or impact, and for each
887 element, which would increase the number of plausible scenarios to accrete the Earth, but
888 could also provide compositional constraints on irreconcilable scenarios, and therefore
889 allow some impactor compositions to be excluded from a given model.

890

891 **6.2. Effect of Moon formation on the Ni/Co ratio in the Earth's mantle**

892 In the previous section we showed that the properties of the magma ocean are model
893 dependent: they have to be inferred from the impactor properties and the final BSE content
894 chosen as a control of the model output. In this section, we infer the viscosity of a magma
895 ocean for one particular model: the Moon formation by an impact with a Mars-sized
896 impactor (Canup, 2004). The Moon forming impactor (named Theia) is believed to be a
897 large Mars-sized impactor which hit the proto-Earth at the end of accretion with an oblique
898 trajectory (Canup & Asphaug, 2001, Canup, 2004). In a simulation of this kind of impact,
899 most of the metal and silicate of the impactor merges with the Earth (Canup, 2004). If we
900 consider mass of the Moon to be negligible compared to that of Theia, and ignore the loss
901 of particles due to the impact, we can determine that the final 10% mass accreted to the

902 Earth was due to the impact with Theia. The core of this impactor is 30% of the total mass
903 of the impactor (Canup, 2004), with the same mean density as the Earth, so it is not
904 improbable that the ratio $R_{core}/R_{impactor}$ is comparable to that of the Earth or Mars today
905 (given by the red and blue vertical lines in Figs. 17). In that case, Eq. (17) and Fig. 17
906 shows that some equilibrium occurred between the magma ocean formed by the impact
907 and the impactor's core sinking into the Earth's core. For every magma ocean viscosity
908 tested here, it is necessary to have interaction between Theia's core and the proto-Earth's
909 mantle to get the final BSE concentration. For a magma ocean viscosity of 0.1 Pa.s, the
910 proto-Earth's Ni/Co ratio is between 0.25 % and 0.45 % lower than the BSE values for a
911 $R_{core}/R_{impactor}$ comparable to those of Mars and the Earth respectively. For a magma ocean
912 viscosity of 100 Pa.s, the proto-Earth Ni/Co ratio is between 1.45% and 3.00 % lower than
913 the BSE values for a $R_{core}/R_{impactor}$ comparable to those of Mars and the Earth, respectively.
914 This means that the Moon forming impact had a significant effect on the BSE Ni/Co ratio,
915 which can be high if the magma ocean formed after the impact was viscous (100 Pa.s) and
916 the core radius of Theia was around 1850 km.

917

918

919 **7. Conclusion**

920 We developed numerical models to characterize the effects of viscosity and partition
921 coefficients on the metal/silicate equilibrium for moderately siderophile elements. We

922 showed that the volume of silicate equilibrated with a small volume of metal is mostly
923 controlled by the partition coefficients and the viscosity of the silicate. The viscosity ratio
924 between metal and silicate is a second order parameter but still has a significant effect.
925 The scope of this study does not include other elements that have different partitioning
926 behavior (V, Cr, Mn etc.) and future models of equilibrium between metal and silicate
927 will have to integrate these elements to get a clearer view of chemical exchanges within
928 the Early Earth. Furthermore, the range of Re and We covered in this study does not cover
929 the whole range of Re and We numbers during the accretion event (Fig. 10). Therefore, in
930 the future, we will need to model more complex flows (such as shown in [Samuel, 2012](#) or
931 [Wacheul et al., 2014](#)), to widen the scope of our interpretations (see Section 4 for the
932 extrapolation conditions). Future models should also account for the thermal equilibration
933 during metal/silicate separation ([Wacheul & Le Bars, 2018](#)) to characterize the effects of
934 temperature on the partition coefficient values. Other phenomena, while important, are
935 ignored due to being beyond the scope of the study, for instance the effect of the droplet
936 size and shape ([Qaddah et al., 2019](#)), or stretch-enhancing diffusion ([Lherm & Deguen,](#)
937 [2018](#)), or the possibility of large core-merging events ([Landeau et al., 2016](#)). All these
938 phenomena are beyond the scope of this study and should be taken into account in further
939 work and models of accretion.
940 Nevertheless, we proposed a parameterization of the disequilibrium between a silicate
941 magma ocean and a metallic droplet for moderately siderophile element behavior. Using

942 this parameterization on Ni and Co behavior at the end of accretion, it is possible to define
943 some constraints on the viscosity of the magma ocean. For a given model of accretion to
944 fit the current BSE concentrations, the viscosity of the magma ocean and the impactor
945 composition need to be changed accordingly: large impactors with large metallic cores
946 ($R_{core} > 1100$ km) and high magma ocean viscosity (10 -100 Pa.s) favor a high degree of
947 metal/silicate equilibrium; while metal/silicate disequilibrium models can be achieved
948 with moderately small metallic cores ($R_{core} \approx 300$ -1000 km) and low viscosity (0.1 - 1
949 Pa.s) magma ocean.

950 When applying our results to the Moon-forming impact, we showed that the current Ni/Co
951 ratio in the BSE is affected by the Moon's formation, depending on the viscosity of the
952 magma ocean formed after the impact. The Moon's formation can account for 0.25 to 0.45
953 % of the final BSE Ni/Co ratio for a low viscosity (0.1 Pa.s) magma ocean, and for 1.45%
954 to 3 % of the final BSE Ni/Co ratio for a high viscosity (100 Pa.s) magma ocean.

955

956 **Acknowledgments**

957 This research received funding from the French PNP program (INSU-CNRS), the
958 French Government Laboratory of Excellence initiative No. ANR-10-LABX- 0006 and
959 the Région Auvergne. This paper is Laboratory of Excellence ClerVolc contribution No.
960 **xxx**. This project has received funding from the European Research Council (ERC)
961 under the European Union’s Horizon 2020 research and innovation programme (grant
962 agreement 681835 FLUDYCO-ERC-2015-CoG). This project has received funding from
963 the European Research Council (ERC) under the European Union’s Horizon 2020
964 research and innovation programme (grant agreement 716429). We thank Renaud
965 Deguen for his fruitful comments.

966

967

968

969 **References**

970 C. J. Allegre, J.-P. Poirier, E. Humler, and A. W. Hofmann. The Chemical composition
971 of the Earth. *Earth and Planetary Science Letters*, 134:515–526, 1995.

972

973 D. Andrault, N. Bolfan-Casanova, G. Lo Nigro, M. A. Bouhifd, G. Garbarino and M.
974 Mezouar. Solidus and liquidus profiles of chondritic mantle: Implication for melting of

975 the Earth across its history. *Earth and planetary science letters*, 304(1-2):251-259,
976 2011.

977

978 M. A. Bouhifd and A.P. Jephcoat. Convergence of Ni and Co metal-silicate partition
979 coefficients in the deep magma-ocean and coupled silicon-oxygen solubility in iron
980 melts at high pressures. *Earth and Planetary Science Letters*, 307(3-4):341–348, 2011.

981

982 M. A. Bouhifd and A.P. Jephcoat. The effect of pressure on partitioning of Ni and Co
983 between silicate and iron-rich metal liquids: a diamond-anvil cell study. *Earth and*
984 *Planetary Science Letters*, 209(1-2):245–255, 2003.

985

986 M.A. Bouhifd, V. Clesi, A. Boujibar, N. Bolfan-Casanova, C. Cartier, T. Hammouda,
987 M. Boyet, G. Manthilake, J. Monteux and D. Andrault. Silicate melts during Earth's
988 core formation. *Chemical Geology*, 461, 128-139, 2017.

989

990 A. Boujibar, D. Andrault, M. A. Bouhifd, N. Bolfan-Casanova, J.-L. Devidal, and N.
991 Trcera. Metal-silicate partitioning of sulphur, new experimental and thermodynamic
992 constraints on planetary accretion. *Earth and Planetary Science Letters*, 391:42– 54,
993 2014.

994 T.H. Burbine, and K.M. O'Brien. Determining the possible building blocks of the Earth
995 and Mars. *Meteoritics & Planetary Science*, 39(5):667-681, 2004.
996
997 C. Cartier, T. Hammouda, M. Boyet, M. A. Bouhifd and J.-L. Devidal. Redox control
998 of the fractionation of niobium and tantalum during planetary accretion and core
999 formation. *Nature Geoscience*, 7(8):573, 2014
1000
1001 R.M. Canup. Simulations of a late lunar-forming impact. *Icarus*, 168(2):433–456,
1002 2004.
1003
1004 R. M. Canup. Accretion of the Earth. *Philosophical Transactions of the Royal Society*
1005 *A: Mathematical, Physical and Engineering Sciences*, 366(1883):4061-4075, 2008.
1006
1007 R. M. Canup, and E. Asphaug. Origin of the Moon in a giant impact near the end of the
1008 Earth's formation. *Nature*, 412(6848):708, 2001.
1009
1010 I. D. Chang. On the wall effect correction of the Stokes drag formula for axially
1011 symmetric bodies moving inside a cylindrical tube. *Zeitschrift für angewandte*
1012 *Mathematik und Physik ZAMP*, 12(1):6-14, 1961.

1013 V. Clesi, M.A. Bouhifd, N. Bolfan-Casanova, G. Manthilake, A. Fabbrizio, and D.
1014 Andraut. Effect of H₂O on metal-silicate partitioning of Ni, Co, V, Cr, Mn and Fe:
1015 Implications for the oxidation state of the Earth and Mars. *Geochimica et*
1016 *Cosmochimica Acta*, 192:97–121, 2016.

1017

1018 J. Crank. *The Mathematics of Diffusion*, 2nd ed. Clarendon Press, Oxford. viii, 414 p,
1019 1975.

1020

1021 T. W. Dahl and D. J. Stevenson. Turbulent mixing of metal and silicate during planet
1022 accretion and interpretation of the Hf-W chronometer. *Earth and Planetary Science*
1023 *Letters*, 295(1-2):177–186, 2010.

1024

1025 N. Dauphas, J. H. Chen, J. Zhang, D. A. Papanastassiou, A. M. Davis, and C.
1026 Travaglio. Calcium-48 isotopic anomalies in bulk chondrites and achondrites: Evidence
1027 for a uniform isotopic reservoir in the inner protoplanetary disk. *Earth and Planetary*
1028 *Science Letters*, 407:96-108, 2014.

1029

1030 R. Deguen, P. Olson, and P. Cardin. Experiments on turbulent metal-silicate mixing in a
1031 magma ocean. *Earth and Planetary Science Letters*, 310(3-4):303–313, 2011

1032

1033 R. Deguen, M. Landeau, and P. Olson. Turbulent metal-silicate mixing, fragmentation,
1034 and equilibration in magma oceans. *Earth and Planetary Science Letters*, 391:274–287,
1035 2014.

1036

1037 M. J. Drake, and K. Righter. Determining the composition of the Earth. *Nature*,
1038 416(6876):39, 2002.

1039

1040 R. A. Fischer, Y. Nakajima, A. J. Campbell, D. J. Frost, D. Harries, F. Langenhorst, N.
1041 Miyajima, K. Pollok, and D. C. Rubie. High pressure metal-silicate partitioning of Ni,
1042 Co, V, Cr, Si, and O. *Geochimica et Cosmochimica Acta*, 167:177–194, 2015.

1043

1044 J. R. Fleck, C. L. Rains, D. S. Weeraratne, C. T. Nguyen, D. M. Brand, S. M Klein, J.
1045 M. McGehee, J. M. Rincon, C. Martinez and P.L Olson. Iron diapirs entrain silicates to
1046 the core and initiate thermochemical plumes. *Nature communications*, 9(1), 71, 2018.

1047

1048 B. Jacobsen, Q.- Z. Yin, F. Moynier, Y. Amelin, A. N. Krot, K. Nagashima, I. D.
1049 Hutcheon, and H. Palme. ^{26}Al - ^{26}Mg and ^{207}Pb - ^{206}Pb systematics of Allende CAIs:
1050 Canonical solar initial $^{26}\text{Al}/^{27}\text{Al}$ ratio reinstated. *Earth and Planetary Science Letters*,
1051 272(1-2):353–364, 2008.

1052

1053 J. H. Jones and M. J. Drake. Geochemical constraints on core formation in the Earth.
1054 *Nature*, 322(6076):221, 1986.

1055

1056 B. B., Karki, D. B., Ghosh, and S. K. Bajgain. Simulation of Silicate Melts Under
1057 Pressure. In *Magma Under Pressure* : 419-453, 2018

1058

1059 B; B. Karki. and L. P. Stixrude. Viscosity of MgSiO₃ liquid at Earth's mantle
1060 conditions: Implications for an early magma ocean. *Science*, 328(5979):740-742, 2010.

1061

1062 Y. Ke and Solomatov, V. S. Coupled core-mantle thermal evolution of early Mars.
1063 *Journal of Geophysical Research: Planets*, 114(E7), 2009

1064

1065 J. D. Kendall and H. J. Melosh. Differentiated planetesimal impacts into a terrestrial
1066 magma ocean: fate of the iron core. *Earth and Planetary Science Letters*, 448:24–33,
1067 2016.

1068

1069 T. Kleine, C. Munker, K. Mezger, and H. Palme. Rapid accretion and early core
1070 formation on asteroids and the terrestrial planets from Hf-W chronometry. *Nature*,
1071 418(6901):952–955, 2002.

1072

1073 T. Kleine, M. Touboul, B. Bourdon, F. Nimmo, K. Mezger, H. Palme, S.B. Jacobsen,
1074 Q.-Z. Yin, and A.N. Halliday. Hf–W chronology of the accretion and early evolution of
1075 asteroids and terrestrial planets. *Geochimica et Cosmochimica Acta*, 73(17):5150–5188,
1076 2009.

1077

1078 T. Kleine and J. F. Rudge. Chronometry of meteorites and the formation of the Earth
1079 and Moon. *Elements*, 7(1):41–46, 2011.

1080

1081 Y. Kono, C. Kenney-Benson, Y. Shibasaki, C. Park, G. Shen, and Y. Wang. High-
1082 pressure viscosity of liquid Fe and FeS revisited by falling sphere viscometry using
1083 ultrafast X-ray imaging. *Physics of the Earth and Planetary Interiors*, 241:57–64, 2015.

1084

1085 M. Landeau, P. Olson, R. Deguen and B. H. Hirsh. Core merging and stratification
1086 following giant impact. *Nature Geoscience*, 9(10):786, 2016.

1087

1088 V. Lherm and R. Deguen. Small-Scale Metal/Silicate Equilibration During Core
1089 Formation: The Influence of Stretching Enhanced Diffusion on Mixing. *Journal of*
1090 *Geophysical Research: Solid Earth*, 123(12):10,496-10,516, 2018.

1091

1092 C. Liebske, B. Schmickler, H. Terasaki, B. T. Poe, A. Suzuki, K. I. Funakoshi, K.i.
1093 Funakochi, R. Ando and D. C. Rubie. Viscosity of peridotite liquid up to 13 GPa:
1094 Implications for magma ocean viscosities. *Earth and Planetary Science Letters*, 240(3-
1095 4):589-604, 2005.

1096

1097 U. Mann, D. J. Frost and D. C. Rubie. Evidence for high-pressure core-mantle
1098 differentiation from the metal–silicate partitioning of lithophile and weakly-siderophile
1099 elements. *Geochimica et Cosmochimica Acta*, 73(24):7360-7386, 2009.

1100

1101 W. F. McDonough. 3.16–Compositional model for the Earth’s core. *Treatise on*
1102 *geochemistry*, :547-568, 2003.

1103

1104 W. F. McDonough and S.-S. Sun. The composition of the Earth. *Chemical Geology*,
1105 (120): 223–253, 1995.

1106

1107 R. C. Mittal and R. K. Jain. Redefined cubic B-splines collocation method for solving
1108 convection–diffusion equations. *Applied Mathematical Modelling*, 36(11)): 5555-5573,
1109 2012.

1110

1111 J. Monteux, Y. Ricard, N. Coltice, F. Dubuffet and M. Ulvrova. A model of metal–
1112 silicate separation on growing planets. *Earth and Planetary Science Letters*, 287(3-
1113 4):353-362, 2009.

1114

1115 J. Monteux, H. Amit, G. Choblet, B. Langlais and G. Tobie. Giant impacts,
1116 heterogeneous mantle heating and a past hemispheric dynamo on Mars. *Physics of the*
1117 *Earth and Planetary Interiors*, 240:114-124, 2015.

1118

1119 G. Morard, J. Siebert, D. Andrault, N. Guignot, G. Garbarino, F. Guyot, F. and D.
1120 Antonangeli. The Earth's core composition from high pressure density measurements of
1121 liquid iron alloys. *Earth and Planetary Science Letters*, 373:169-178, 2013.

1122

1123 M. Nakajima and D. J. Stevenson. Melting and mixing states of the Earth's mantle after
1124 the Moon-forming impact. *Earth and Planetary Science Letters*, 427:286-295, 2015

1125

1126 D. P. O'Brien, A. Morbidelli and H.F. Levison. Terrestrial planet formation with strong
1127 dynamical friction. *Icarus*, 184(1):39-58, 2006.

1128

1129 E. Olsson, and G. Kreiss. A conservative level set method for two phase flow. *Journal*
1130 *of computational physics*, 210(1):225-246, 2005.

1131

1132 B. Qaddah, J. Monteux, V. Clesi, M. A. Bouhifd and M. Le Bars. Dynamics and
1133 stability of an iron drop falling in a magma ocean. *Physics of the Earth and Planetary*
1134 *Interiors*, 289:75-89, 2019.

1135

1136 B. Qaddah, J. Monteux and M. Le Bars. Thermal evolution of a metal drop falling in a
1137 less dense, more viscous fluid. *Physical Review Fluids*, 5(5): 053801, 2020.

1138

1139 N. Rai, and W. van Westrenen. Core-mantle differentiation in Mars. *Journal of*
1140 *Geophysical Research: Planets*, 118(6):1195-1203, 2013.

1141

1142 Y. Ricard, O. Šrámek, and F. Dubuffet. A multi-phase model of runaway core-
1143 mantle's segregation in planetary embryos. *Earth and Planetary Science Letters*, 284(1-
1144 2):144–150, 2009.

1145

1146 K. Righter. Prediction of metal-silicate partition coefficients for siderophile elements:
1147 An update and assessment of P-T conditions for metal-silicate equilibrium during
1148 accretion of the Earth. *Earth and Planetary Science Letters*, 304(1-2):158–167, 2011.

1149

1150 D. C. Rubie, D.J. Frost, U. Mann, Y. Asahara, F. Nimmo, K. Tsuno, P. Kegler, A.
1151 Holzheid, and H. Palme. Heterogeneous accretion, composition and core-mantle
1152 differentiation of the Earth. *Earth and Planetary Science Letters*, 301(1-2):31–42,
1153 2011.

1154

1155 D.C. Rubie, H.J. Melosh, J.E. Reid, C. Liebske, and K. Righter. Mechanisms of metal-
1156 silicate equilibration in the terrestrial magma ocean. *Earth and Planetary Science*
1157 *Letters*, 205(3-4): 239–255, 2003.

1158

1159 D.C. Rubie, S.A. Jacobson, A. Morbidelli, D.P. O’Brien, E.D. Young, J. de Vries, F.
1160 Nimmo, H. Palme, and D.J. Frost. Accretion and differentiation of the terrestrial planets
1161 with implications for the compositions of early-formed Solar System bodies and
1162 accretion of water. *Icarus*, 248:89–108, 2015.

1163

1164 J. F. Rudge, T. Kleine, and B. Bourdon. Broad bounds on Earth’s accretion and core
1165 formation constrained by geochemical models. *Nature Geoscience*, 3(6):439–443,
1166 2010.

1167

1168 H. Samuel and P. J. Tackley. Dynamics of core formation and equilibration by negative
1169 diapirism. *Geochemistry, Geophysics, Geosystems*, 9(6), 2008.

1170

1171 H. Samuel. A re-evaluation of metal diapir breakup and equilibration in terrestrial
1172 magma oceans. *Earth and Planetary Science Letters*, 313-314:105–114, 2012.

1173 E. M. Shoemaker. Interpretation of lunar craters. *Physics and Astronomy of the Moon* :
1174 283-359, 1962

1175

1176 J. Siebert, J. Badro, D. Antonangeli, and F. J. Ryerson. Metal-silicate partitioning of Ni
1177 and Co in a deep magma ocean. *Earth and Planetary Science Letters*, 321-322:189–
1178 197, 2012.

1179

1180 D.J. Stevenson. Models of the Earth’s core. *Science*, 214(4521):611–619, 1981.

1181

1182 M. Ulvrová, N. Coltice, Y. Ricard, S. Labrosse, F. Dubuffet, J. Velínský, and O.
1183 Šrámek. Compositional and thermal equilibration of particles, drops, and diapirs in
1184 geophysical flows. *Geochemistry, Geophysics, Geosystems*, 12(10), 2011.

1185

1186 O. Šrámek., Y. Ricard, and F. Dubuffet. A multiphase model of core formation.
1187 *Geophysical Journal International*, 181(1):198–220, 2010.

1188

1189 J.-B. Wacheul and M. Le Bars. Fall and fragmentation of liquid metal in a viscous
1190 fluid. *Physical Review Fluids*, 2(9):090507, 2017.

1191

1192 J.-B. Wacheul and M. Le Bars. Experiments on fragmentation and thermo-chemical
1193 exchanges during planetary core formation. *Physics of the Earth and Planetary*
1194 *Interiors*, 276:134-144, 2018.

1195

1196 J.-B. Wacheul, M. Le Bars, J. Monteux, and J. M. Aurnou. Laboratory experiments on
1197 the breakup of liquid metal diapirs. *Earth and Planetary Science Letters*, 403: 236–245,
1198 2014.

1199

1200 K.J. Walsh, A. Morbidelli, S.N. Raymond, D.P. O’Brien, and A.M. Mandell. A low
1201 mass for mars from Jupiter’s early gas-driven migration. *Nature*, 475(7355):206–209,
1202 2011.

1203

1204 G. W. Wetherill. Occurrence of giant impacts during the growth of the terrestrial
1205 planets. *Science*, 228(4701):877-879, 1985.

1206

1207 J. Wade and B. J. Wood. Core formation and the oxidation state of the Earth. *Earth and*
1208 *Planetary Science Letters*, 236(1-2):78-95, 2005.

1209

1210 B. J. Wood, M. J. Walter, and J. Wade. Accretion of the Earth and segregation of its
1211 core. *Nature*, 441(7095):825–833, 2006.

1212

1213 B. J. Wood, J. Wade, and M. R. Kilburn. Core formation and the oxidation state of the
1214 Earth: Additional constraints from Nb, V and Cr partitioning. *Geochimica et*
1215 *Cosmochimica Acta*, 72(5):1415–1426, 2008.

1216

1217

1218 **Captions of Figures and Tables**

1219 **Figure 1:** Schematics of core-mantle segregation. First, the impactor (metal+silicate)
1220 enters a turbulent magma ocean. The impactor is fragmented and melted on impacting the
1221 surface of the proto-planet. The metallic phase then forms a diapir which, if the magma
1222 ocean is turbulent enough, fragments into a cloud of droplets ranging in size from a few
1223 millimeters to 10 cm maximum (Rubie et al., 2011; Deguen et al, 2014; Wacheul et al.,
1224 2014; Wacheul and Le Bars, 2017,2018). Each droplet interacts with the surrounding
1225 silicate, exchanging heat and chemical elements, until it reaches thermo-chemical
1226 equilibrium with its environment.

1227

1228 **Figure 2:** Schematic representation of the initial conditions and geometry of our models.
1229 The characteristics of the metal and silicate phases are listed respectively in red and black.
1230 The boundary conditions are detailed in blue (top), solid red line (side), green (bottom and
1231 global conditions). The red arrow illustrates the symmetry axis (red dotted line) used to
1232 define the 3D output.

1233 **Figure 3:** Evolution of the metallic volume ratio ($V_{\text{calculated}}/V_{\text{theoretical}}$) during a simulation
1234 for different h_{max} values, for a silicate viscosity of 100 Pa.s. The colored and dashed line
1235 represent the evolution of $V_{\text{calculated}}/V_{\text{theoretical}}$ for different mesh sizes with time. The scale
1236 at the top shows the distance traveled by the diapir over a given time.

1237 **Figure 4:** Evolution of the velocity field, r-component (on the left) and z-component (on
1238 the right), for different widths of computational domain. Widths vary from $2x R_{Fe}$ to $6x$
1239 R_{Fe} . The chosen width for the simulations is $5xR_{Fe}$. Note that the results presented here
1240 are calibration runs, with a height of $30xR_{Fe}$. The same simulations have been performed
1241 at varying heights, leading to a final height of $28x R_{Fe}$ (see Fig. 2 for the calibrated
1242 geometry).

1243 **Figure 5:** Evolution of the volume fraction of the silicate during the simulation. When
1244 equal to 1 (red), the fluid is a silicate, when equal to 0 (blue) the fluid is a metal. The limit
1245 between metal and silicate is the black line between the red and blue parts ($\Phi_{ls} = 0.5$). The
1246 time necessary for the diapir to reach the distance of $10R_{Fe}$ is 12.1 s.

1247

1248 **Figure 6:** Evolution of adimensional concentration of the siderophile element in the
1249 silicate, for a partition coefficient $D^{met/sil} = 1$. For clarity purposes the metal is shown by
1250 the grey area surrounded by a black line. The black line is the boundary between metal
1251 and silicate and defines the surface where the exchange reaction happens. The
1252 adimensional concentration is given by the following formula given in Eq. (9). In this case
1253 $X_{sil}^0 = 10^{-5}$, $X_{met}^0 = 0.2$ and $D^{met/sil} = 1$, and the chemical Peclet number is $Pe \sim 800$.

1254

1255 **Figure 7:** Evolution of the volume of silicate undergoing reaction during the simulation.
1256 In red, the volume of silicate affected chemically. In blue, the volume of silicate unaffected
1257 by the passage of the diapir. The metal is colored in grey. The ratio R_C defined in the study
1258 corresponds to the volume of the red areas divided by the total volume of silicate (red +
1259 blue areas).

1260

1261 **Figure 8:** Evolution of R_C as a function of time in the reference case defined in the text
1262 ($\mu_{sil} = \mu_{met} = 100$ Pa.s). The four lines illustrate four different values of $D^{met/sil}$ ranging from
1263 1 (black) to 10^3 (blue).

1264

1265 **Figure 9:** Evolution of the time necessary for the diapir to move through $10R_{Fe}$ as a
1266 function of the silicate viscosity. Black points are the values corresponding to each
1267 study. The red area corresponds to Stokes flows, and the blue area to intermediate
1268 flows. The clusters of black points correspond to the variation in velocity due to the
1269 variation in metal viscosity. The theoretical values are plotted in red and derived from
1270 equations (9) and (10). Typical times of diapir equilibrium, from [Wacheul et al. \(2014\)](#),
1271 are shown in blue. The size of the marker is scaled logarithmically on the chemical
1272 Peclet number, ranging from 8 (smallest) to 3000 (largest).

1273

1274 **Figure 10:** On the left: Re as a function of We obtained from our numerical simulations
1275 (one red circle for each calculation). The blue area shows the Intermediate regime flow,
1276 and the red area the Stokes regime flow. The dashed area illustrates the domain where
1277 diapirs are stable. On the right: Comparison between the geologically plausible values of
1278 We and Re for the Earth's magma ocean and the values covered by our study.

1279

1280 **Figure 11:** Evolution of R_C as a function of Re during the sinking of a 1cm-radius droplet
1281 for an adimensional time of 1. The Stokes flow regime (red area) and intermediate flow
1282 regime (blue area) are separated by a black vertical line at $Re=1$. The dot color
1283 characterizes different values for $D^{met/sil}$ ranging from 1 to 10^3 . The size of the marker is
1284 scaled logarithmically on the chemical Peclet number, ranging from 8 (smallest) to 3000
1285 (largest).

1286 **Figure 12:** Evolution of R_C as a function of R_μ for 5 different metallic viscosities (shown
1287 in the 5 boxes), different values of $D^{met/sil}$ and obtained at a distance of $10R_{Fe}$. From top
1288 left to bottom panel the metallic viscosity increases from 0.1 Pa.s to 1000 Pa.s. The silicate
1289 viscosities corresponding to R_μ are indicated on the top x-axis. The size of the marker is
1290 scaled logarithmically with the chemical Peclet number, ranging from 8 (smallest) to 3000
1291 (largest).

1292

1293 **Figure 13:** Evolution of $\log R_C$ as a function of the normalized surface (left panel) and
 1294 evolution of the normalized surface as a function of R_μ (right panel) for models with μ_{silicate}
 1295 $= 0.1 \text{ Pa.s}$ for the reference time defined in Fig. 9. The normalized surface of the diapir is
 1296 the surface of the diapir in the simulation divided by $S_{\text{theoretical}} = 4\pi R_{\text{Fe}}^2$ (initial surface of
 1297 the sphere).

1298 **Figure 14:** $\log R_C$ calculated from the parameterization of Eq (11) vs $\log R_C$ obtained from
 1299 the simulations. The red line is the 1:1 line (perfect fit), and the dashed lines bound the 5σ
 1300 confidence interval.

1301

1302 **Figure 15:** Mantle fraction chemically contaminated by a moderately siderophile element
 1303 after metallic core fragmentation as a function of the impactor size. In these figures we
 1304 compute Eqs. 6, 11 and 12 using $R_{\text{Fe}}=1\text{cm}$, $v_{\text{diapir}}=v_{\text{stokes}}$ and $\mu_{\text{met}}=0.1 \text{ Pa.s}$. The left panel
 1305 shows the influence of the partition coefficient for a fixed viscosity ratio $R_\mu=1$. The right
 1306 panel shows the influence of the viscosity ratio for a fixed partition coefficient
 1307 $D^{\text{met/sil}}=100$.

1308

1309 **Figure 16:** Evolution of Ni/Co ratio in the mantle after an impact as a function of the
 1310 impactor size for different silicate viscosities (0.1 to 100 Pa.s). We represent here the
 1311 variation of the Ni/Co ratio after the impact relative to the initial BSE concentration:

1312
$$\Delta \left(\frac{\text{Ni}}{\text{Co}} \right) = 100 \times \frac{\left(\frac{\text{Ni}}{\text{Co}} \right)_{\text{Final}} - \left(\frac{\text{Ni}}{\text{Co}} \right)_{\text{BSE}}}{\left(\frac{\text{Ni}}{\text{Co}} \right)_{\text{BSE}}}$$
. Since the impact happens on the BSE, the more the

1313 Ni/Co ratio is different to that of the BSE, the more the impactor has reached equilibrium.

1314

1315 **Figure 17:** Ni/Co ratio in the Earth’s mantle before equilibration with the core of an
1316 impactor corresponding to 10% of the Earth’s mass as a function of the radius of the
1317 impactor’s core normalized to the impactor size and for different magma ocean viscosities.

1318 The $R_{\text{core}}/R_{\text{Earth}}$ current ratio is shown by the blue dashed line, and the $R_{\text{core}}/R_{\text{Mars}}$ ratio by
1319 a red dashed line. In the calculation, the impactor is the same size as Mars ($R_{\text{impactor}} = 3390$
1320 km), and the impactor core radius ranges from 340 km to 2040 km. We represent here the
1321 variation in Ni/Co ratio before the impact relative to the BSE concentration but for a well-

1322 mixed mantle after impact:
$$\Delta \left(\frac{\text{Ni}}{\text{Co}} \right) = 100 \times \frac{\left(\frac{\text{Ni}}{\text{Co}} \right)_{\text{post-impact}} - \left(\frac{\text{Ni}}{\text{Co}} \right)_{\text{BSE}}}{\left(\frac{\text{Ni}}{\text{Co}} \right)_{\text{BSE}}}.$$

1323

1324 **Table 1:** Parameters and variables used in this study. When values are not given, the
1325 variable is calculated later in the text (according to the specific case).

1326

1327 **Table 2.** Values of fitted parameters for Eq. 11 using the least-square methods. The errors
1328 associated with the value are given by the 1σ error value. The data used for
1329 parameterization are the same as the data presented in sections 3.3 and 3.4. The
1330 comparison between calculated values from Eq. 11 and the values obtained after
1331 simulation is presented in Fig. 13.

1332

1333 **Table 1**

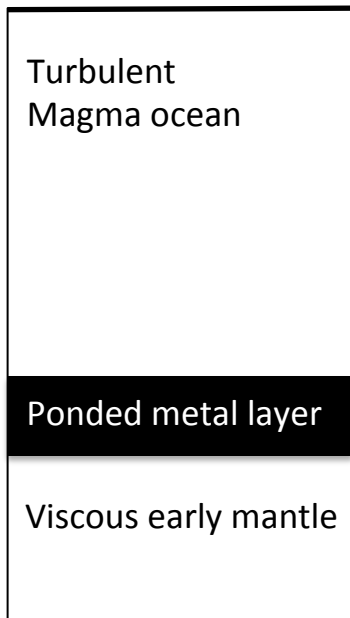
Parameter	Name	Values in this study
All models		
ρ	Density of the fluid	silicate: 3300 - metal: 8000 kg.m ⁻³
t	Time	0.6 - 125 s
\mathbf{u}	Velocity vector	m.s ⁻¹
R_{Fe}	Radius of the diapir	1 cm
h_{max}	Maximum unit cell size	0.1 $\times R_{\text{Fe}}$
Two-phase flow		
P	Dynamic Pressure of the fluid	1 atm
μ	Dynamic viscosity of the fluid	10 ⁻¹ – 10 ³ Pa.s
g	Acceleration of gravity	9.81 m.s ⁻²
l	Distance fluid - initial interface	m
F_{st}	Surface tension force	Calculated for $\sigma = 1 \text{ N.m}^{-1}$, in N.m ⁻³
Φ	Volume fraction of the fluid	silicate: $\Phi = 0$ metal: $\Phi = 1$ no unit
ϵ_{ls}	Parameter controlling interface reinitialization	$h_{\text{max}}/2$

γ	Parameter controlling velocity reinitialization	0.001 – 0.3 m.s ⁻¹
Transport of Diluted Species		
c_i	Concentration of element i	mol.m ⁻³
k_c	Diffusion coefficient of element i	10 ⁻⁶ m ² .s ⁻¹
R_i	Reaction rate for element i	mol.m ⁻³ .s ⁻¹
N_i	Molar flux of element i	0 mol.m ⁻² .s ⁻¹
Scaling of the study		
Re	Reynolds number	2.5×10 ⁻⁵ to 110
We	Weber number	2.3×10 ⁻⁵ to 3.5
R_μ	Viscosity ratio (= μ_{met}/μ_{sil})	10 ⁻⁴ to 10 ⁴
R_C	Ratio of the silicate volume reacted	see Section 3

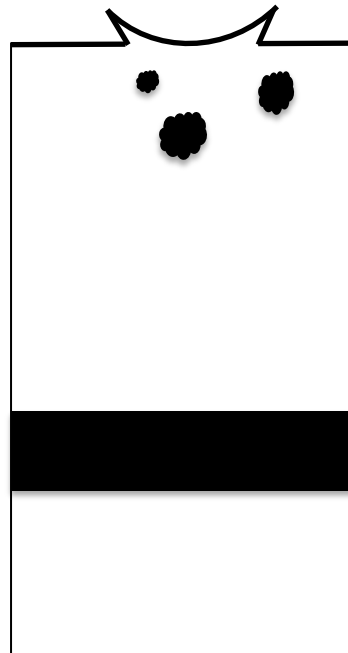
1334

1335 **Table 2**

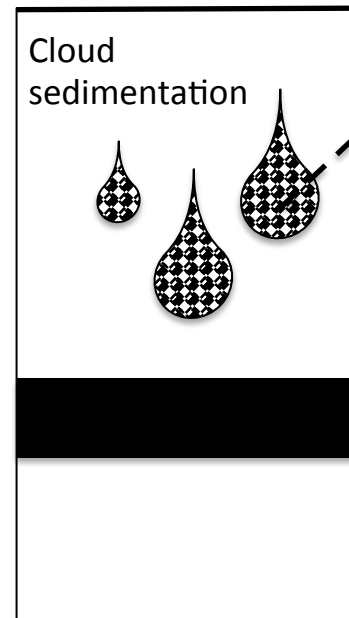
Parameters	a ($D_{met/sil}$)	b (Re)	c (R_μ)	d
Values	-0.235	-0.283	0.011	-1.686
1 σ	0.02	0.03	0.001	0.07



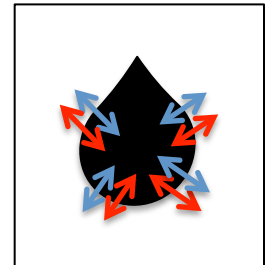
Impact fragmentation



Cloud sedimentation



Iron droplet



Thermo-
chemical
exchanges

